Incidence Angle Normalization of C-Band Radar Backscattering Coefficient over Agricultural Surfaces Using Dynamic Cosine Method

Sami Najem, Nicolas Baghdadi, Hassan Bazzi, Mehrez Zribi

remote sensing

MDPI

Article

Incidence Angle Normalization of C-Band Radar Backscattering Coefficient over Agricultural Surfaces Using Dynamic Cosine Method

Sami Najem [1], Nicolas Baghdadi [1,*], Hassan Bazzi [1] and Mehrez Zribi [2]

[1] National Research Institute for Agriculture, Food and Environment (INRAE), UMR TETIS, University of Montpellier, 500 Rue François Breton, 34093 Montpellier, CEDEX 5, France; sami.najem@inrae.fr (S.N.)
[2] CESBIO, UT3, CNES, CNRS, INRAE, IRD, 18 Avenue Edouard Belin, 31401 Toulouse, France
* Correspondence: nicolas.baghdadi@teledetection.fr

Abstract: The radar-backscattering coefficient (σ^0) depends on surface characteristics and instrumental parameters (wavelength, polarization, and incidence angle). For Sentinel-1 (S1), with incidence angles ranging from 25° to 45°, σ^0 for similar targets typically differs by a few dB depending on their localization in the S1 swath. Overcoming this angular dependence is crucial for the operational applications of radar data. In theory, σ^0 follows a cosine function with an exponent "N" that represents the degree of dependence between σ^0 and the incidence angle. In order to reduce the effect of the incidence angle on σ^0, dynamic N normalizations based on vegetation descriptors, NDVI and SAR Ratio (VV/VH), were applied and then compared to the results obtained with temporally fixed N normalizations. N was estimated at each S1 date during the period of the study for three main summer crops: corn, soybean, and sunflower. Analysis shows that the angular dependence of the S1 σ^0 is similar for all three crops. N varies from 3.0 for low NDVI values to 2.0 for high NDVI values (stage of maximal vegetation development) in the VV polarization and from 2.5 to 1.5 for the VH polarization. Furthermore, N fluctuates strongly during the periods before plant emergence and after harvesting, due to variations in the soil roughness. Finally, the results demonstrated that the dynamic normalization of σ^0 significantly reduces its angular dependence compared to fixed N (N = 1 and N = 2), with SAR ratio-based normalization performing similarly to NDVI-based normalization.

Keywords: SAR; Sentinel-1; incidence angle; normalization

Citation: Najem, S.; Baghdadi, N.; Bazzi, H.; Zribi, M. Incidence Angle Normalization of C-Band Radar Backscattering Coefficient over Agricultural Surfaces Using Dynamic Cosine Method. *Remote Sens.* **2024**, *16*, 3838. https://doi.org/10.3390/rs16203838

Academic Editor: Sang-Eun Park

Received: 5 September 2024
Revised: 8 October 2024
Accepted: 14 October 2024
Published: 16 October 2024

1. Introduction

Synthetic aperture radar (SAR) remote sensing has become a cornerstone in Earth observation, particularly with the advent of advanced satellite systems like those used in the Copernicus Sentinel-1 (S1) mission. The S1 constellation offers high temporal frequencies, with an optimal revisit time of 6 days before January 2022 and 12 days from January 2022 onwards, as well as a high temporal resolution with a pixel spacing of 10 m by 10 m, allowing for earth surface monitoring at very small scales. S1 C-band SAR data operate at a frequency of 5.405 GHz and interact with surface features on the surface of the Earth. The data used in this study are the S1 IW (Interferometric Wide-swath), which boast a swath of around 250 km and an incidence angle ranging approximately from 25° to 45°. A notable advantage of SAR remote sensing data over optical remote sensing data is that they are impervious to cloud coverage, as the SAR is not affected by cloud cover [1,2]. This opens the door for continuous earth observations throughout the year, regardless of atmospheric conditions. Thanks to these qualities, SAR data are used for a variety of purposes, including land cover classification, target detection, and the retrieval of land surface parameters such as soil moisture, snow water equivalent, etc. [3–8].

However, the backscattering coefficient (σ^0) of SAR remote sensing data is dependent on the incidence angle (θ) [9–11]. Thus, analyzing SAR images could be complicated due to

the fact that S1 satellites observe a given swath of the Earth surface from different incidence angles (the closest point to the satellite has a smaller incidence angle than the farthest point). In addition, observations of the Earth are conducted according to many orbits, interacting with a given point on the Earth's surface from different incidence angles. In the scientific literature, the angular dependence over icy surfaces was shown to vary between 0.07 and 0.25 dB/1° [12–14] for S1 C-band data and 0.26 dB/1° for Radarsat C-band data [15]. Furthermore, angular dependence is related to factors such as land cover, crop type, crop development, and soil roughness [16–18]. This observed angular dependence could have a major impact when using S1 data, especially when working over a large swath with a wide range of incidence angles, where there could be a significant difference between the backscattering coefficients for the same surface characteristics caused solely by differences in the incidence angle [13,18]. This could hinder some sensitive applications such as land cover classification and crop detection over larger areas. For this reason, a normalization is usually applied to SAR data with the aim of reducing the effect of the incidence angle on the backscattering coefficient, enabling the use of mapping approaches that are not hampered by angular dependence, though the transferability generally depends on other factors as well, such as climatic conditions and agricultural practices.

There are many methods used for incidence angle normalization in the scientific literature; for example, the semi-empirical model-based approach [19–21], the linear method [22,23], the histogram method [17], and the cosine method [18,24–26]. The semi-empirical radiometric correction of the slope effect uses either single-model or multi-model techniques, with multimodal approaches performing the best. The main inconvenience of this approach is that it requires calculations that are more rigorous, and more data compared to other methods. The linear method employs a simple linear equation for backscattering coefficient normalization. The main disadvantage of this method is that it oversimplifies the relationship between the backscattering coefficient and the incidence angle and needs a lot of a priori information before application, leading to a heterogeneous performance across different surfaces, sites, and climates. The histogram method is based on the construction of histograms of radar backscatter coefficients across varying incidence angles; a normalization coefficient is then derived and applied to standardize the data. The advantage of this method is that it requires little a priori information. However, its disadvantage is that the results can appear discontinuous across the area of the acquisition. Finally, the cosine method is one of the most widely used normalization methods; it is based on the principle that the backscattering coefficient follows a cosine-dependent function with the incidence angle [27]. It is widely used because it requires very little a priori information and is relatively more user-friendly compared to other methods. The cosine method assumes that the relationship between σ^0 and θ is based on Lambert's law for optics [24]. Generally, the cosine exponent (N) used is fixed as either N = 1 (first order) or N = 2 (cosine-squared). In the case of highly reflective surfaces, N = 2 generally provides good results. However, the cosine exponent (N) can change depending on the characteristics of the observed land surface [26,28–30]. For instance, N was found to be equal to 6.3 for VV polarization and 5.5 for HH polarization over fields of olive trees for the C-band [29], and it ranged from 2.1 to 2.8 for VV polarization and from 1.4 to 2.2 for VH polarization in wetland areas [30]. In flooded forest biomes, N was shown to range from 0.24 to 1.73 and 1.42 to 3.36 in the case of savannahs for L-band data in HH polarization [26]. Therefore, N was shown to have a wide range of values depending on the land surface. Furthermore, for stable surfaces that do not show a major change through time, such as ice sheets, forests, and permanent grasslands, the degree of dependence between σ^0 and θ is generally constant, whereas N is not stable for surfaces that show high dynamism through time, such as croplands [31]. Over these surfaces, N varies throughout the growth cycle according to the stage of development (plowing, sowing, vegetation development, etc. [18,32,33]. Feng et al. showed that, over corn croplands, N depends mainly on vegetation characteristics (N as a function of NDVI) and is affected by soil roughness but not by soil moisture [18]. They found that, for corn croplands, N values ranged from around 1.0 to 9.0 for VV and from around 1.0 to 6.0 for

VH; N was highest after sowing, when vegetation is low and the soil roughness is at its lowest values. Therefore, vegetation indices can be used in order to estimate and improve N. The NDVI (Normalized Difference Vegetation Index) is one of the most widely used vegetation indices calculated from optical remote sensing. It correlates with vegetation biomass and photosynthetic activity, where higher values indicate increased vegetation density and productivity, reflecting more photosynthetically active radiation absorption and near-infrared reflectance [34,35]. NDVI was used in order to enhance the normalization of σ^0 from the S1 C-band over corn fields in China, outperforming the cosine-squared method by 53% [18]. However, NDVI relies on optical data; it could be unreliable whenever there is cloud cover. One way of overcoming this potential issue is by using the SAR Ratio (VV/VH), which is a widely used vegetation index [36–39] based solely on SAR data. The SAR Ratio was shown to have a highly significant correlation with corn plant height [36] and a Pearson's correlation of 0.65 and 0.41 with dry biomass for canola and soybean, respectively [37]. Furthermore, the SAR Ratio was shown to correlate well with NDVI over wheat fields [38].

Given this information, this study investigates how the backscattering coefficient (σ^0) varies with the incidence angle (θ) for different summer crops (sunflower, soybean, and corn). It also evaluates the effectiveness of using cosine methods for angle normalization using dynamic N based on NDVI compared to a fixed N normalization (N = 1 and N = 2) in order to improve the widely used cosine method. To overcome the cloud cover limitations associated with optical remote sensing and ensure the timely and continuous calculation of the dynamic N values throughout the year, the study then proposes computing dynamic N values using the SAR ratio (VV/VH) as an alternative vegetation descriptor to the common optically derived vegetation indices (NDVI). The results highlighted the effectiveness of using dynamic N values compared to a fixed N normalization. SAR ratio-based normalization showed comparable results to optical-derived N normalization, which guarantees operational SAR-based normalization without the need for complementary optical data.

2. Materials and Methods

2.1. Study Area

Our study area is located near the city of Pau and stretches across two French regions, namely Nouvelle-Aquitaine and Occitanie, in the southwest of France. It lies within the oceanic climate zone that dominates the west of France, receiving 1000 mm of annual rainfall. The temperature generally varies between 2° and 26° depending on the seasons. The area is around 6000 km^2 (100 km × 60 km), encompassing 2500 km^2 of agricultural lands (croplands), according to the farmer's declarations of the year 2021 (https://geoservices.ign.fr/rpg, accessed on 1 May 2024). Corn, soybean, and sunflower (the three main summer crops) occupied around 60% of the total cultivated area, with 43,000, 5200, and 4600 fields, respectively. Figure 1 shows the location of the study site and the land cover/land use of the area, obtained from Copernicus Global Land Cover (accessed through https://land.copernicus.eu/en/products/corine-land-cover, accessed on 1 May 2024).

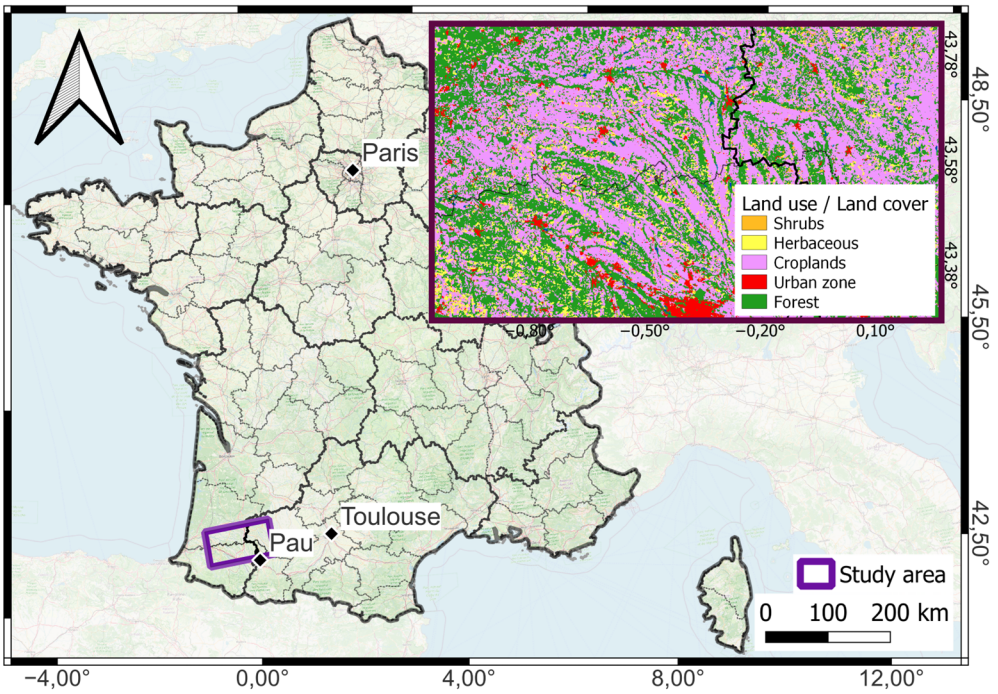

Figure 1. Location of the study area.

2.2. Datasets

2.2.1. Sentinel-1 Data

Sentinel-1 (S1) synthetic aperture radar (SAR) data were obtained in the C-band at a frequency of 5.405 GHz, corresponding to a wavelength of 5.55 cm, and feature a pixel spacing of 10 m. The S1 constellation originally consisted of two satellites, Sentinel-1A (S1A) and Sentinel-1B (S1B). The S1 constellation provided data with a 6-day revisit interval, until the mission ended for S1B in December 2021. Consequently, only S1A has been operational since then, and the revisit time changed to a 12-day interval from January 2022 onwards. For this study, S1 data spanning 1 April 2021 to 30 November 2021 were used.

S1 Acquisitions are available in "ascending" (evening at 18:00 UT) and "descending" (morning at 06:00 UT) modes. The Level 1 ground range-detected (GRD) product, which includes VV and VH polarizations, was utilized for this research. The S1 data were supplied by the European Space Agency (ESA) and are freely available on the Copernicus data distribution platform (https://browser.dataspace.copernicus.eu, accessed on 1 May 2024). The acquired S1 data were calibrated using the ESA S1 toolbox. Initially, a radiometric calibration was applied to convert the data from the digital number (DN) format to the backscattering coefficient σ^0 in linear units. Following this, a geometric correction was executed in order to address the systemic distortions arising from the sensor's viewing angle and the distortions that occur due to terrain topography. This was applied using a digital elevation model with 30 m resolution from the shuttle radar topography mission for topographic referencing.

For every S1 acquisition, pixel values within each field were averaged to derive a single value representing the mean backscattering coefficient for that field. Both the VV and VH polarizations were used in this study. Additionally, we created a channel derived from the existing SAR polarizations called the SAR Ratio. In decibel unites, the SAR Ratio is the difference between the VV (dB) and VH (dB) polarizations ($SAR\ Ratio = \sigma_i^0\mathrm{VV(dB)} - \sigma_i^0\mathrm{VH(dB)}$).

Figure 2 shows the spatial distribution of the orbits used in the study. Three descending as well as three ascending orbits were used. The intersections between the different ascending and the three descending orbits are represented as hatched zones, covering the western and eastern sections of the study area. These intersection zones will be used in the calculation of the difference in the backscattering coefficient between the orbits ($\Delta\sigma_{\theta i}^0$)

in future sections. Within these hatched zones, the number of corn fields was 15,000, the number of soybean fields was 3000, and the number of sunflower fields was 2000.

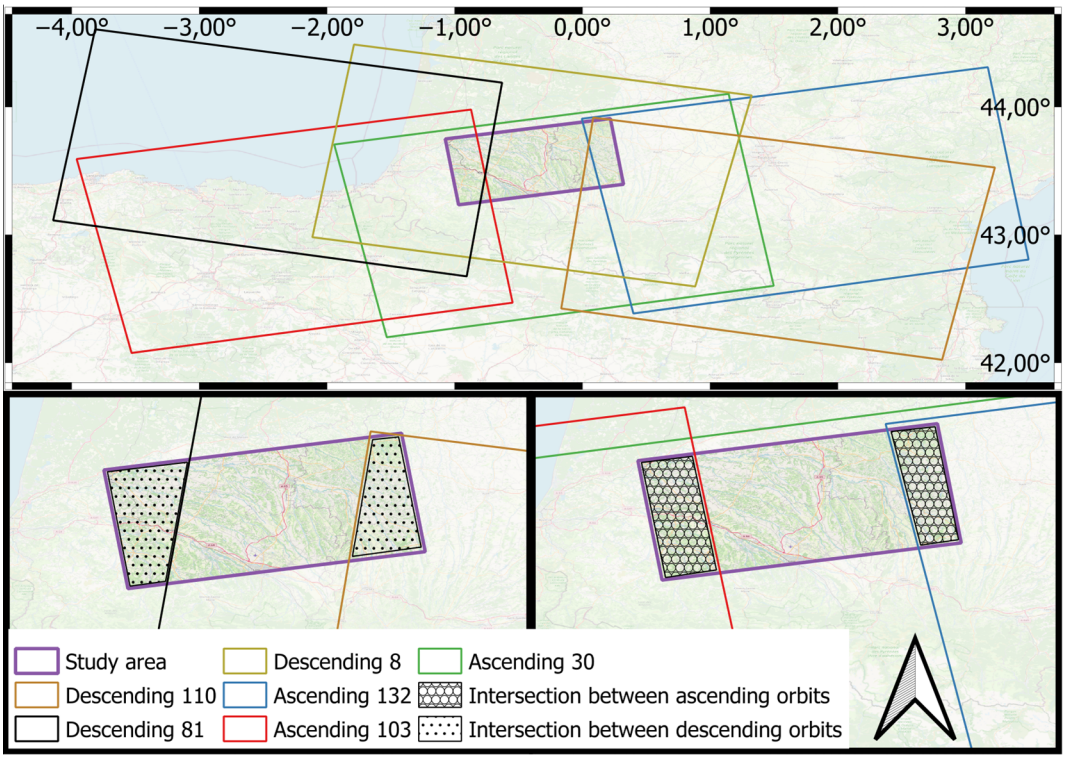

Figure 2. All the orbits used in the study and the intersections between the ascending orbits, as well as the descending orbits. N will be estimated using only data from the hatched zones. The satellites in the S1 constellation are right-looking. Therefore, descending orbits have smaller incidence angles on their east side and greater incidence angles on their west side, while ascending orbits have a smaller incidence angle on the west side and a greater incidence on their east side.

Figure 3 shows the temporal distribution of the S1 acquisitions from the different orbits used in this study. It shows that there is a time difference of 24 h between the acquisitions of the descending 81 (D81) and descending (D8) orbits, and 24 h between D8 and D110. Similarly, we can see that there is a 24 h time difference between the sequential ascending orbits A103, A30, and A132. Furthermore, when examining the time difference between the ascending and the descending orbits, we can see a time difference between 1.5 days and 3.5 days.

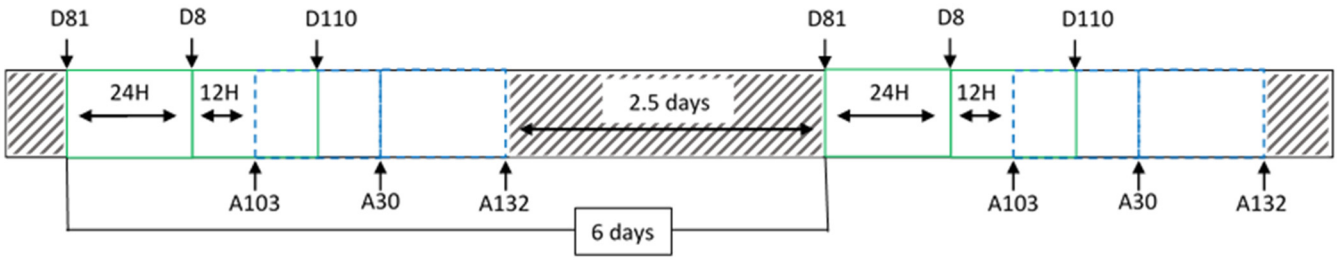

Figure 3. Temporal distribution of the S1 orbits used in this study. D81 = descending 81; D8 = descending 8; A103 = ascending 103; D110 = descending 110; A30 = ascending 30; A132 = ascending 13.

Figure 4 shows an S1 acquisition over our study area on 7 July 2021 for orbit D8. The incidence angle values show a decrease from west to east (Figure 4a), while the backscat-

tering coefficient shows an increase in values from west to east (Figure 4b), reflecting the angular dependence of the Sentinel-1 data [24,30].

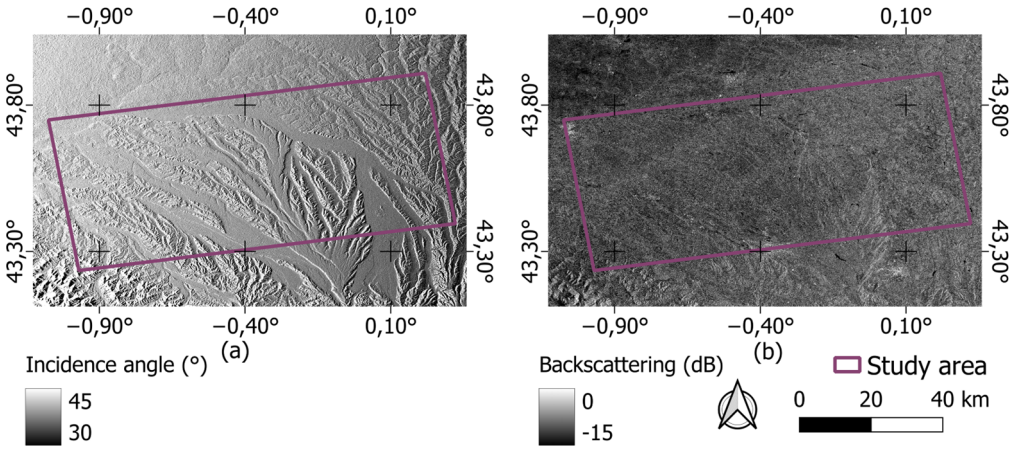

Figure 4. An S1 acquisition for the D8 orbit over our study area for the date 7 July 2021, showing (**a**) the incidence angle (high values in the west) and (**b**) the backscattering coefficient in VV polarization (lower values in the west). Coordinates are represented in decimal degrees.

2.2.2. Sentinel-2 Data

The Sentinel-2 satellite constellation is part of the European Space Agency's (ESA) Copernicus program and can be accessed freely on the Copernicus data distribution platform (https://browser.dataspace.copernicus.eu). The constellation comprises two identical satellites, Sentinel-2A and Sentinel-2B, which capture high-resolution multispectral images of the Earth's surface, providing images at a revisit time of 5 days. The Sentinel-2 data cover 13 spectral bands from visible to short-wave infrared, with spatial resolutions of 10 m, 20 m, and 60 m depending on the specific band. S2 data were sourced from the Theia platform (https://www.theia-land.fr/), which offers processed Sentinel-2 (S2) data, with corrections for atmospheric disturbances. Cloud-free images from 1 April 2021 to 30 November 2021 were downloaded over our study area. These optical data (10 m bands) were subsequently utilized to calculate the Normalized Difference Vegetation Index (NDVI). For every image, NDVI values were obtained for each field by averaging the pixels within said field.

2.2.3. ERA-5 Land Precipitation Data

This study used precipitation data from the ERA5-Land dataset. The ERA5 dataset, provided by Copernicus and representing the fifth generation of the atmospheric reanalysis developed by ECMWF, spans the period from 1950 up to three months before the present. This reanalysis combines actual weather observations with modeled data worldwide to create a comprehensive, consistent, and globally accessible climate dataset. ERA5-Land, a subset of ERA5, focuses on land components and derives its atmospheric forcing from the near-surface meteorological conditions and flux parameters of ERA5, specifically from its lowest model level (level 137), which is 10 m above the ground. Key parameters such as downward shortwave and longwave radiation, along with total precipitation (both liquid and solid), were used to linearly interpolate ERA5 data to the higher spatial resolution of ERA5-Land, improving it from approximately 30 km × 30 km (ERA5) to around 9 km × 9 km (ERA5-Land).

2.3. Normalization Method

2.3.1. Angular Dependence of the S1 Backscattering Coefficient

The most commonly used normalization approaches were derived from Lambert's law for optics. The model is based on the assumption that the amount of power that is re-radiated in the upper hemisphere follows a cosine law [24,30]. The backscattering coefficient σ^0 is dependent on the incidence angle (θ). The relationship between σ^0 and θ

follows a cosine function; therefore, the measured backscatter σ^0_θ is expressed as follows (in linear unit):

$$\sigma^0_\theta = a\, cos^N(\theta) \quad (1)$$

The coefficient *a* is related to the target's backscattering properties, and N depends on the dominant scattering mechanism and sensor condition [40]. Therefore, over the agricultural area, N has to be calculated at different stages of development for each crop. Seeing that the backscattering coefficient $\sigma^0_{\theta i}$ follows Equation (1) at every incidence angle (θ_i), the backscattering coefficient can be normalized (σ^0_{norm}) at a given reference angle (θ_{norm}) as follows:

$$\sigma^0_{norm} = \sigma^0_{\theta i}\left(\frac{\cos\theta_{norm}}{\cos\theta_i}\right)^N \quad (2)$$

A fixed N (N = 1 and N = 2) throughout the year is the most frequently used in the literature [25,26]. The first-order cosine method employs N = 1; this is applied over tropical forest land covers. The cosine squared method (N = 2) performs well for ideal surfaces that exhibit a high diffusion rate. However, in the case of agricultural fields, the land's surface exhibits great temporal variability, caused by three main factors, namely vegetation cover, soil moisture, and surface roughness. Unfortunately, this variability is not accounted for when using a fixed N. Therefore, a dynamic N would be more suitable for accommodating the variations in the surface throughout the growing season. In this paper, N will be calculated for the main summer crop types present in our study site (sunflower, soybean, corn). In addition, N will be modeled using one vegetation descriptor derived from optical images (NDVI) and another calculated from S1 SAR images (SAR ratio).

2.3.2. N Value Estimation

Given that N varies throughout the growth cycle based on the developmental stage of the crop [18], we will estimate N at each acquisition date with the aim of understanding the dynamic of N. The most commonly employed method for estimating N assumes that, at the time of a given SAR acquisition, fields of the same crop exhibit uniform characteristics. However, this assumption is not always valid, particularly given that a Sentinel-1 image spans a swath of approximately 250 km. Within such an extensive area, variations in soil preparation and sowing dates, crop growth rates, and soil moisture are to be expected due to the differing weather conditions and agricultural practices across the region. In order to address these limitations, this study proposes the use of two closely timed ascending or descending orbits at a time (with orbit 1 and orbit 2 never being separated by more than 24 h) to analyze the angular dependence of the backscatter coefficient (σ^0) over the same field. We only utilized orbit pairs from the same orbital mode (either exclusively ascending or exclusively descending) because certain crops, such as sunflower, exhibit distinct behaviors between ascending and descending modes [41]. Specifically, the orbit couples used were (D81, D8), (D8, D110), (A103, A30), and (A30, A132). Our hypothesis supposes that soil moisture between the paired images remains relatively consistent if no rainfall occurs during the 24 h period separating the two images. To ensure similar soil moisture conditions, ERA-5 Land data were used in order to eliminate the effect of rainfall events by using only images acquired during rain-free periods between 3 days before the acquisition date of D81 and the acquisition date of A132. This choice of 3 days before D81 acquisition was made because a rainfall event affects the C-band backscattering for up to 3 days [42,43]. Consequently, the observed differences in σ^0 values for a given field between the two acquisition dates are attributed solely to variations in the incidence angle through the assumption that soil roughness remains consistent within a 24 h period between two acquisitions and that vegetation growth is negligible over this short time span.

For a given field, the difference in the backscattering coefficient ($\Delta\sigma^0$) between two orbits (two ascending or two descending orbits), separated by only 24 h, is expressed as follows:

$$\Delta\sigma^0(\text{dB}) = \sigma^0_{\theta 1}(\text{dB}) - \sigma^0_{\theta 2}(\text{dB}) \quad (3)$$

$\sigma^0_{\theta 1}$ is the backscattering coefficient value from the first orbit used at incidence angle θ_1 and $\sigma^0_{\theta 2}$ is the backscattering coefficient value from the second orbit used at incidence angle θ_2, both in decibel units. The first orbit is always the one with the greater θ. As a result of the previously discussed safeguards that were set in place, the coefficient *a* over a given field is assumed to be the same for the two orbits used. Consequently, Equation (3) can be developed using Equation (1):

$$\Delta\sigma^0(\mathrm{dB}) \;=\; \mathrm{N} \times [10 \times \log(\cos\theta_1) - 10 \times \log(\cos\theta_2)] \tag{4}$$

Using Equation (4), we calculated the value of N for each crop (sunflower, corn, and soybean) at each acquisition date (the acquisition date of one of the six orbits was used as the reference date) and for both polarizations. The cosine-based curve could then be represented by a linear relationship between $\Delta\sigma^0$ (dB) and $10log(\cos\theta_i) - 10log(\cos\theta_i)$, with a slope equal to N, expressed as follows:

$$\mathrm{Y} \;=\; \mathrm{N} \times \mathrm{X} \tag{5}$$

2.3.3. Construction of the Relationship between N and Vegetation Descriptors

After the estimation of N values for each date, a relationship was constructed between N and the vegetation descriptors used in this study (NDVI and SAR ratio). These regression relationships were used to calculate the dynamic N for each field at each date. The relationship will be based on the following linear regression equation:

$$\mathrm{N} \;=\; \mathrm{b} \times \mathrm{VD} + \mathrm{c} \tag{6}$$

with *b* representing the slope, VD (Vegetation Descriptor) representing the vegetation descriptor used (either NDVI or SAR ratio), and *c* representing the intercept.

Three approaches were employed in this study; two examine the relationship between N and NDVI, called the NDVI single-equation and NDVI dual-equation, while the third examines the relationship between N and the SAR ratio.

In the first NDVI-based approach, called the NDVI single-equation approach, the relationship between N and NDVI was constructed using the complete time series (from 1 April 2021 to 30 November 2021).

In addition to the NDVI single-equation approach, a second NDVI-based approach was also assessed, called the NDVI dual-equation approach, where the time series were split into two sections based on the date of the maximum NDVI. This second NDVI-based approach examines the effect of splitting the datasets on the correlation between N and NDVI (which is expected to be higher than when using the complete series of N and NDVI values), and the consequent effect on dynamic normalization. For corn and soybean, the maximum of the average NDVI for these two crops in our area was around 1 September 2021, while for sunflower, the maximum NDVI was around 1 August 2021; therefore, the time series were split as follows:

- Before the date of maximum NDVI: from 1 April 2021 to the date of the maximum average NDVI (1 August 2021 and 1 September 2021, respectively, for sunflower and for the two other crops (corn and soybean)). The regression relationship was established using only data from this range of dates.
- After the date of maximum NDVI: from 1 August 2021 to 1 September 2021, respectively, for sunflower and for the two other crops (corn and soybean) to 30 November 2021. The regression relationship was established using only data in this range of dates.

In addition to the NDVI-based dynamic N values, we propose the use of the SAR ratio as a vegetation descriptor given its strong relationship with vegetation development [36–39]. Using the SAR ratio instead of the NDVI guarantees the continuous production of N values independent of the weather conditions. Thus, in this third approach, called the SAR ratio-based approach, the relationship between N and VV/VH was constructed using the

complete time series (from 1 April 2021 to 30 November 2021). All the aforementioned equations are summarized in Table 1.

Table 1. Formulas used to construct relationships between N and the vegetation descriptors.

Approach	Formulas
NDVI single-equation	$N = b \times NDVI + c$
Dual-equation NDVI	$\begin{cases} N = b1 \times NDVI + c1 \text{ for NDVI before peak} \\ N = b2 \times NDVI + c2 \text{ for NDVI after peak} \end{cases}$
SAR Ratio	$N = b' \times SAR\_ratio + c'$

3. Results

3.1. Estimated Ns

Figure 5 shows how N was estimated at different dates for the corn crop (the two other crops showed similar behavior), with each representing a certain soil condition and/or plant development stage. Figure 5a shows the earliest acquisition, taking place on 2 April 2021, exemplifying a date with no plant activity and no soil work, with N = 2.44. Figure 5b shows N = 4.93 for the date 20 May 2021, in the period before plant emergence. Figure 5c,d represent the dates 7 July 2021 and 30 August 2021, corresponding to early and maximum vegetation development for the corn crop, with N = 1.93 and N = 1.33, respectively. Figure 5e shows an N = 2.76 near the end of plant development (around harvesting date). Finally, Figure 5f shows N = 2.65 after harvesting.

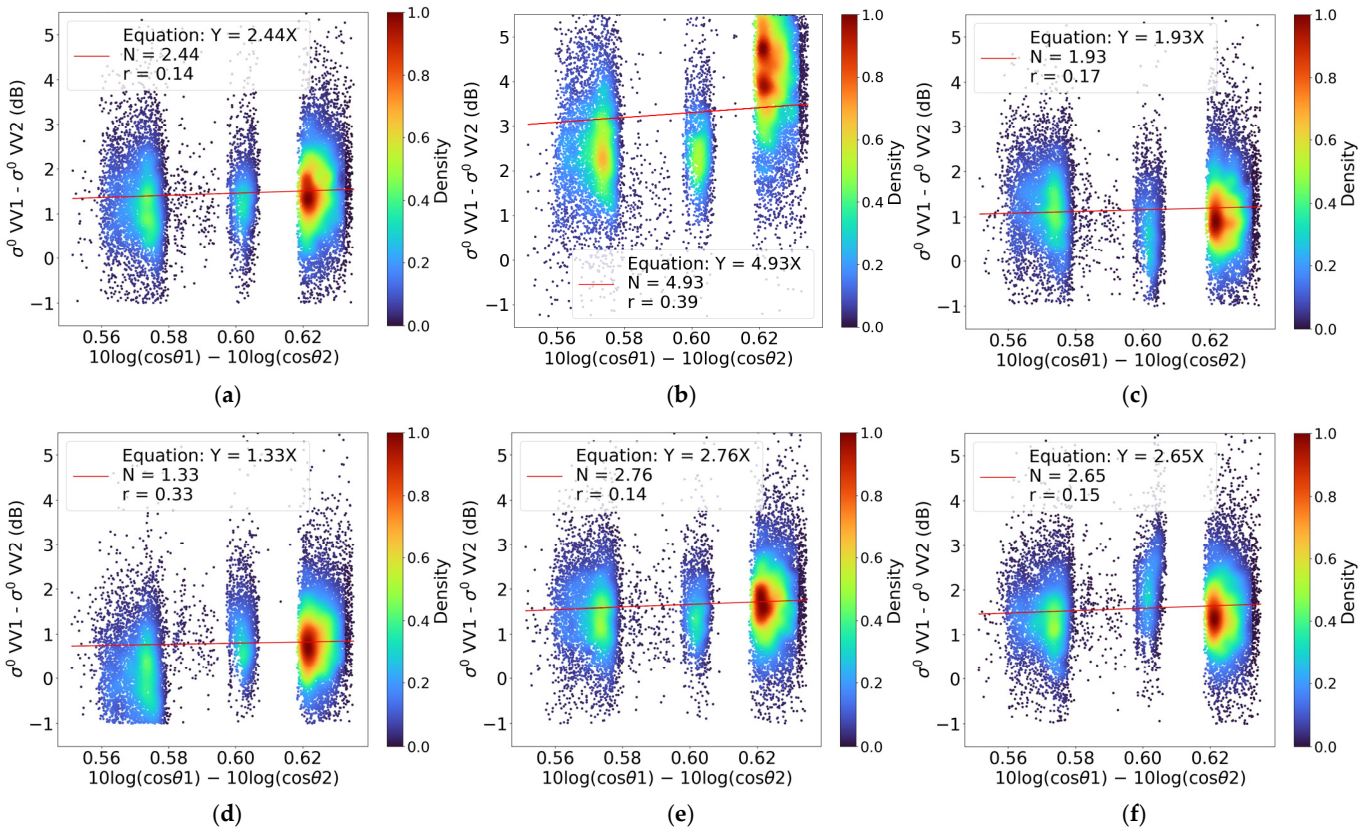

Figure 5. Scatter plots showing examples of the regression relationship used to determine N for the corn crop. (**a**) 2 April 2021: no activity; (**b**) 20 May 2021: soil work; (**c**) 7 July 2021: early plant development; (**d**) 5 September 2021: strong plant development; (**e**) 11 October 2021: harvest; (**f**) 4 November 2021: post-harvest. The clustering observed along the *x*-axis is due to only from the intersection zones being used to estimate N. This leads to a sharp delimitation when calculating *x*-axis values.

Figure 6 shows the estimated values of N at every acquisition date; it also shows the dynamic between N and vegetation indices for each of the summer crops in the study area (corn, soybean, sunflower). The NDVI and the SAR ratio (dB) are the vegetation indices used as indicators of crop development. The values of N vary greatly throughout the year: between 1.5 and around 5.0 for the VV polarization and between 1.0 and 5.5 for the VH polarization. This variation in N is caused by two factors—vegetation cover and soil roughness [18]—both of which are related to agricultural activity. Figure 6a,b shows that for our summer crops, as the vegetation develops, the value of N drops until they reach their lowest, at around 1.5 for VV and around 1.0 for VH, when NDVI is at around its highest.

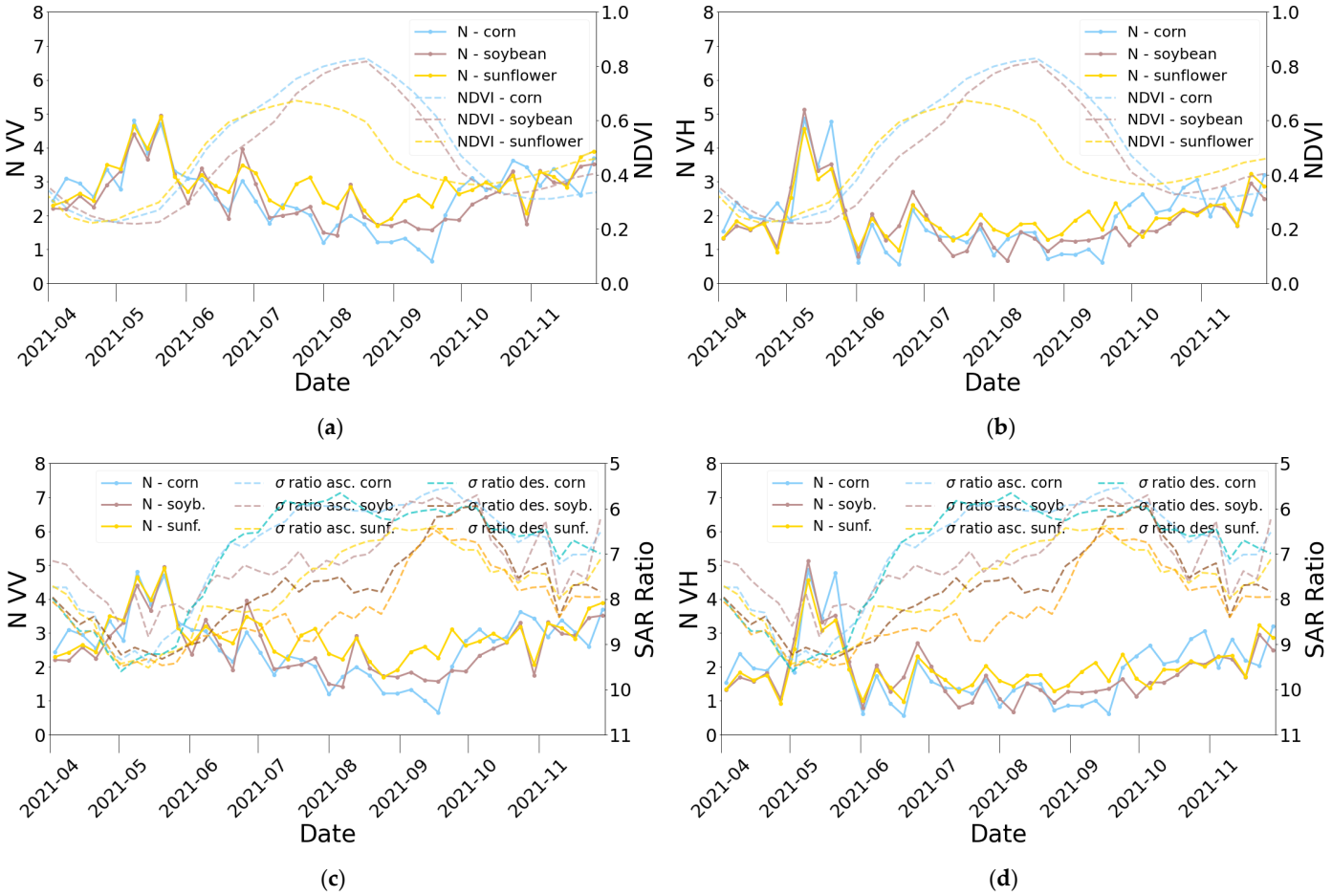

Figure 6. Time series of N throughout the growth cycle of the three summer crops in this study (corn, sunflower, soybean). (**a**) Time series of N for the VV polarization with mean NDVI (of all fields of the same crop); (**b**) time series of N for VV polarization with mean NDVI; (**c**) time series of N for VV polarization with mean SAR ratio (VV − VH); (**d**) time series of N for VV polarization with mean SAR ratio. soyb. = soybean; sunf. = sunflower; asc. = ascending; Des. = descending. The *Y*-axis for the SAR Ratio is inversed for better visualization.

Therefore, N is greater when NDVI is lower for both VV and VH polarizations. Furthermore, we can see that N reaches its maximum value in the month of May, a period that corresponds to seeded fields where soil roughness is generally very low.

Figure 6c,d show the time series of N according to the SAR Ratio. Since there are ascending and descending orbits over our study area, these figures show the average SAR Ratio time series for one ascending orbit (asc.) and one ascending orbit (des.). The N and SAR Ratio are proportional, with N values being greater when the SAR Ratio is greater.

3.2. Dynamic N Relationships

As laid out in Section 2.3.3, the relationships between N values and vegetation descriptors (NDVI and SAR ratio) are established between N and the vegetation descriptors based on the equations found in Table 1. Figure 7a,b show the linear regression for the NDVI single-equation approach in the VV polarization and VH polarization, respectively. The linear regression relationship for VV is N = −2.79 NDVI + 3.97, and the relationship for VH is N = −2.38 NDVI + 2.98.

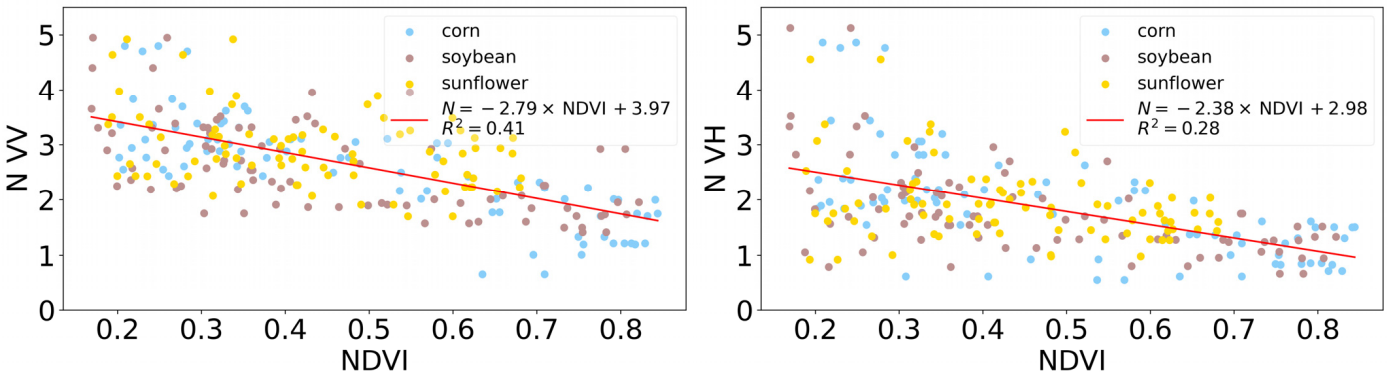

Figure 7. Relationships between N values and NDVI in the case of the NDVI single-equation approach: (**a**) VV polarization; (**b**) VH polarization.

The regression relationships in the case of the dual-equation approach are shown in Figure 8. There are two regression relationships for each polarization (VV and VH): one before the maximum NDVI and one after the maximum NDVI. The relationships are as follows:

- Before the date of the maximum NDVI: The linear regression relationships between N and NDVI for the VV polarization before and after the maximum NDVI, expressed as N = −2.59 NDVI + 3.96 and N = −3.61 NDVI + 4.24, respectively (Figure 8a,b).
- After the date of maximum NDVI: The relationships between N and NDVI before and after the maximum NDVI for the VH polarization, expressed as N = −2.30 NDVI + 2.91 and N = −2.65 NDVI + 3.14, respectively (Figure 8c,d).

The lower correlations between N and NDVI during the first half of the crop cycle, illustrated in Figures 8a and 8c (VV and VH, respectively), are due to the effect of soil roughness, which strongly influences N; N is low before plowing, then high during sowing, and finally low again after the sowing period. Generally, the correlation values are higher for the NDVI dual-equation than for the NDVI single-equation.

The third approach for determining N was based on the SAR Ratio and so the relationship between N and SAR Ratio was also established using the linear regression equation found in Table 1. The SAR ratio data from all the available orbits were used in the process of fitting N with the SAR ratio (three ascending and three descending orbits), resulting in there being six times more points than in the case of NDVI. Figure 9a,b shows the result of this fitting for VV and for VH, respectively, expressed as N = 0.40 SAR Ratio−0.38 and N = 0.26 SAR Ratio−0.11.

Table 2 summarizes the regression relationships found for the three approaches used: N = f(NDVI single-equation), N = f(NDVI dual-equation), and N = f(SAR Ratio).

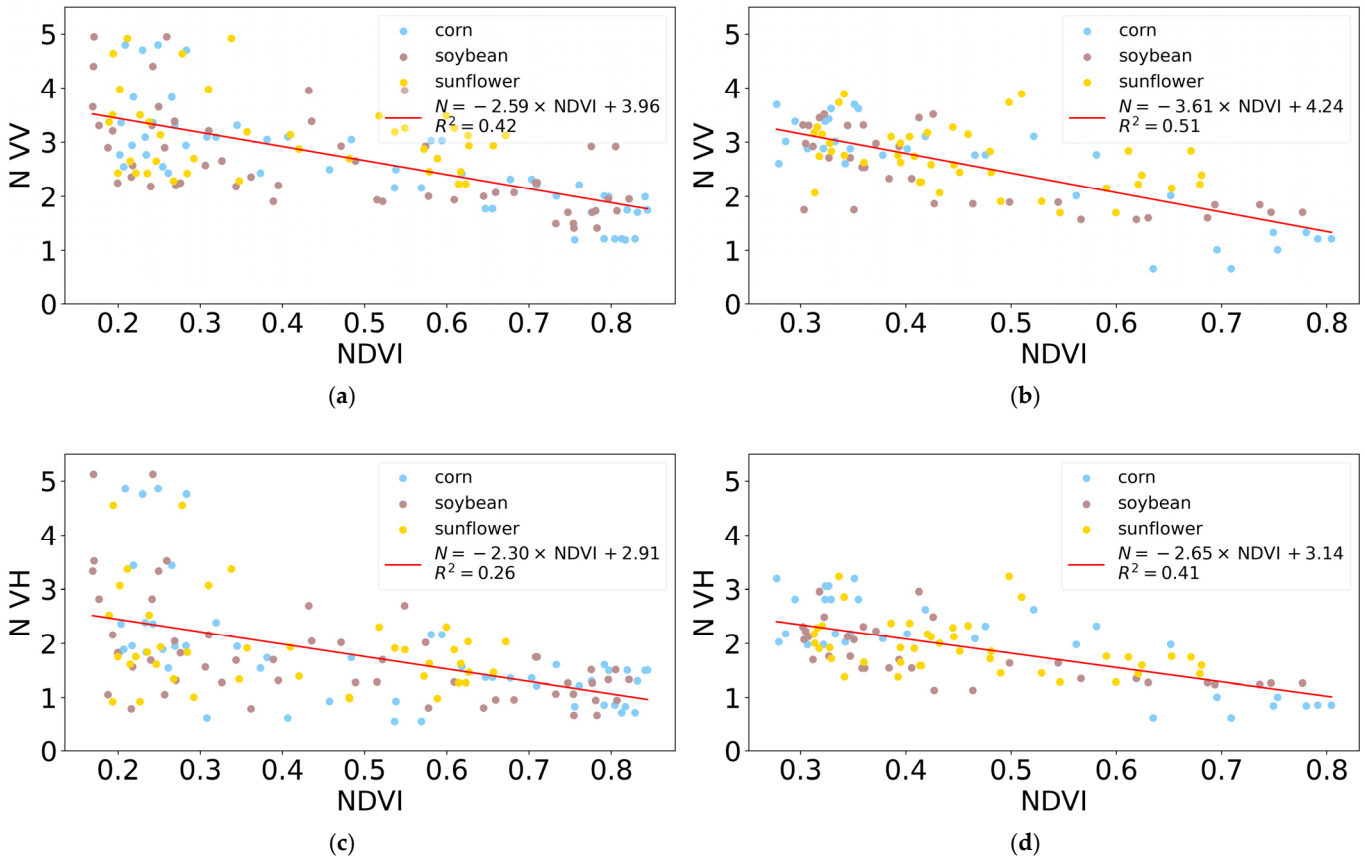

Figure 8. Linear regression relationship between N values and NDVI (**a**) for VV polarization before maximum NDVI, (**b**) for VV polarization after maximum NDVI, (**c**) for VH polarization before maximum NDVI, and (**d**) for VH polarization after maximum NDVI.

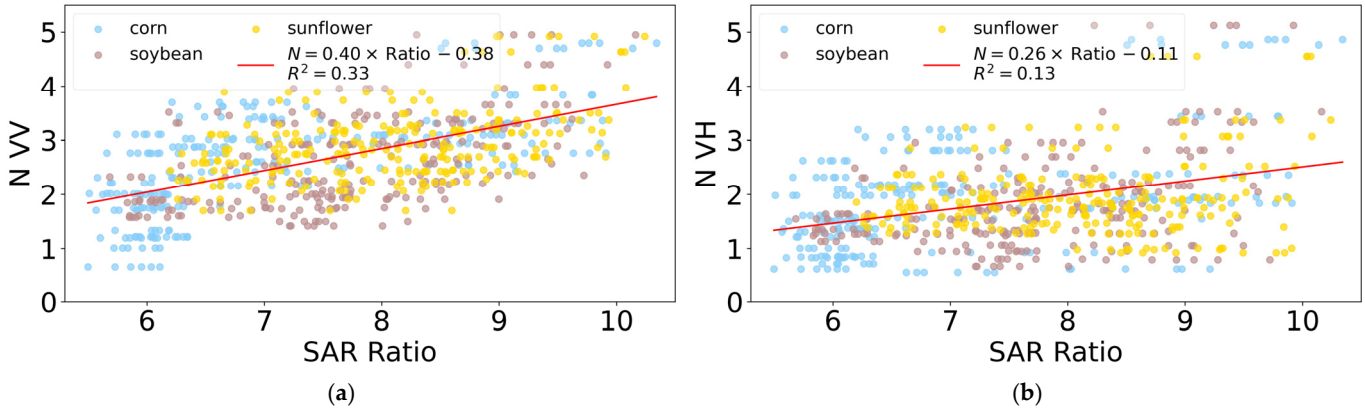

Figure 9. Linear regression relationship between N values and SAR Ratio (**a**) for VV polarization and (**b**) for VH polarization.

Table 2. Regression relationship for the determination of the dynamic N applied for the three summer crops in the area.

Approach	VV	R^2	VH	R^2
NDVI single equation	$N = -2.79\,NDVI + 3.97$	0.41	$N = -2.38\,NDVI + 2.98$	0.28
Dual equation before maximum NDVI	$N = -2.59\,NDVI + 3.96$	0.42	$N = -2.30\,NDVI + 2.91$	0.26
Dual equation after maximum NDVI	$N = -3.61\,NDVI + 4.24$	0.51	$N = -2.65\,NDVI + 3.14$	0.41
SAR Ratio	$N = 0.40\,SAR\_Ratio - 0.38$	0.33	$N = 0.26\,SAR\_Ratio - 0.11$	0.13

3.3. Normalization of S1 Data

Thematic applications using the entirety of an S1 image (250 km swath) sometimes require normalization of the radar backscattering coefficient in order to reduce the effect of the incidence angle. In fact, the first pixel of the S1 image has an incidence of around 25°, while the last pixel has an incidence of around 45°. Generally, the backscattering coefficients of the S1 images are normalized according to Equation (2) using a reference incidence angle (θ_{norm}) corresponding to the center of the S1 swath. To that extent, successful normalization strongly reduces the dependence of the backscattering coefficient with the incidence angle and brings the backscattering coefficients acquired at different incidence angles closer to the backscattering coefficient at θ_{norm}.

In addition to the three dynamic N approaches presented in Section 3.1, we also examined the two fixed N approaches, N = 1 and N = 2. For all dynamic N approaches, N was determined for each field using its NDVI value or its SAR Ratio (Table 1) using the corresponding equations derived in Section 3.1; then, the S1 data were normalized accordingly. In the case of the NDVI dual-equation approach, the selection of the regression relationship to be used was based on the date of maximum NDVI for each field. Orbits D8 and A30 encompass the entirety of the study area; hence, they were normalized to a reference angle of $\theta_{norm} = 39°$ and $\theta_{norm} = 37°$, respectively, the centers of our area for the D8 and A30 orbits.

In order to illustrate the effect of normalization using the different approaches, three key dates were examined for the D8 orbit in Figure 10 (the results for the A30 orbit are in the Appendix A). Figure 10a shows the median σ^0 VV of all fields within each range of incidence angle before and after normalization. Each row represents an approach used for the determination of N, corresponding to fixed N = 1, fixed N = 2, dynamic N = f(NDVI single-equation), dynamic N = f(NDVI dual-equation), and dynamic N = f(SAR Ratio), respectively, results for orbit A30 in Appendix A.

The results show that, for N = 1, the normalized data show a very slight movement towards the reference value ($\sigma^0{}_{VV}$ at the reference normalization angle used ($\theta_{norm} = 39°$)), showing a very small reduction in the angular dependence. For N = 2, the normalized data are closer to the reference value than for N = 1. However, using dynamic N-based approaches leads to better results from all three dynamic N approaches, with the normalized data moving closer to the reference value σ^0_{ref} than they did when using fixed N approaches.

The results for VH polarization (Figure 10b) tell a similar story to the VV polarization, with N = 2, performing better than N = 1, while dynamic N-based normalization approaches still yield better results than when using fixed N.

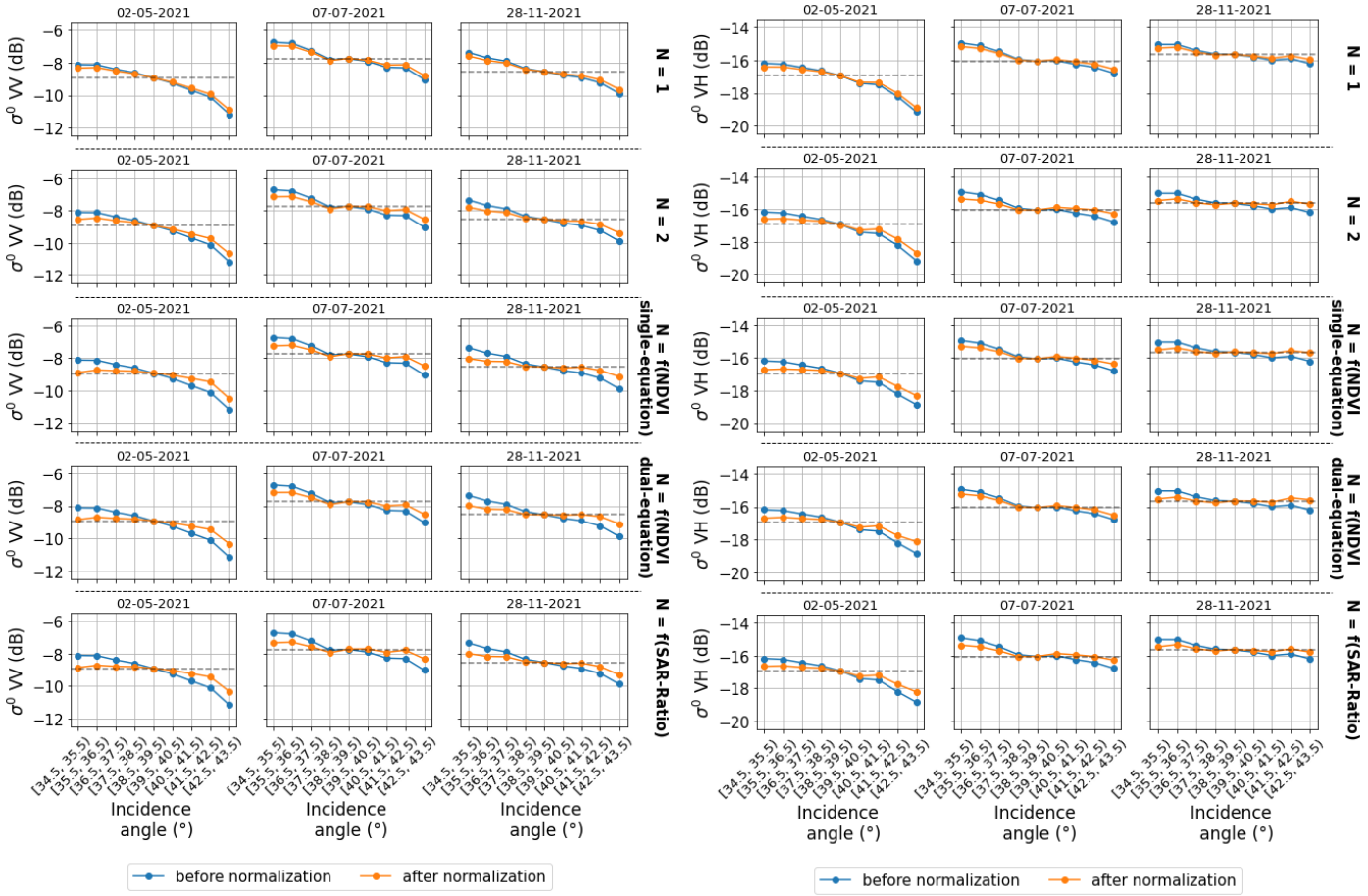

Figure 10. Comparison of the backscattering coefficient before and after normalization to θ_{norm} = 39° for orbit D8. Each approach used is presented in a different row: fixed N = 1; fixed N = 2; N = f(NDVI single-equation); N = f(NDVI dual-equation); N = (SAR Ratio). The dotted line corresponds to $\sigma^0(\theta=39°)$ (called σ^0_{ref}). (**a**): VV; (**b**): VH. Results for orbit A30 in Appendix A.

4. Discussion

Figure 10 shows the effect of normalization when using the different approaches. After normalization, the backscattering coefficient is closer to the reference value σ^0_{ref} (=σ^0 at θ = 39°) at the different incidence angles. However, even after normalization, there may still be a difference between the normalized backscattering coefficient (σ^0_{norm}) and the reference value (σ^0_{ref}). Subsequently, in order to evaluate the effect of normalization on the backscattering coefficient, firstly, the mean of the absolute value of the difference between the two was calculated via the range of incidence angle using all the dates in the period of our study (from 1 April 2021 to 30 November 2021) for the different N approaches used (Figure 11). Figure 11 shows the mean difference between σ^0_{norm} and the σ^0_{ref} for orbit D8 in VV polarization. The difference before normalization is shown as N = 0. Comparing the different normalization approaches shows that N = 1 exhibited the highest difference, reaching an average difference of 0.77 dB, followed by N = 2 with a difference of 0.68 dB. On the other hand, the dynamic N approaches consistently outperformed the fixed N. This is marked by a reduction in the angular dependence of around 40% (for an incidence delta around 4°, between the center = 39°, and the edge = 43°) in the difference between σ^0_{norm} and σ^0_{ref} for dynamic N (for N = f(SAR Ratio, for the range [42.5°, 43.5°)) over the non-normalized data (from 0.86 dB to 0.53 dB), making it higher than that of N = 2, at around 25% (for the range [34.5°, 35.5°)). Figure 11b corroborates the findings of Figure 11a

but for the VH polarization, with the dynamic N showing an improvement of around 40% over the non-normalized data (N = f(NDVI single equation, for the range [34.5°, 35.5°)), compared to around 25% for N = 2 (for the range [34.5°, 35.5°)). This means that the dynamic N-based normalization is more capable of overcoming the effect of the incidence angle when compared to the fixed N-based normalization. Comparing the NDVI based normalization and the SAR based normalization, the findings demonstrate that the SAR ratio-based normalization performs similarly to the NDVI-based normalizations.

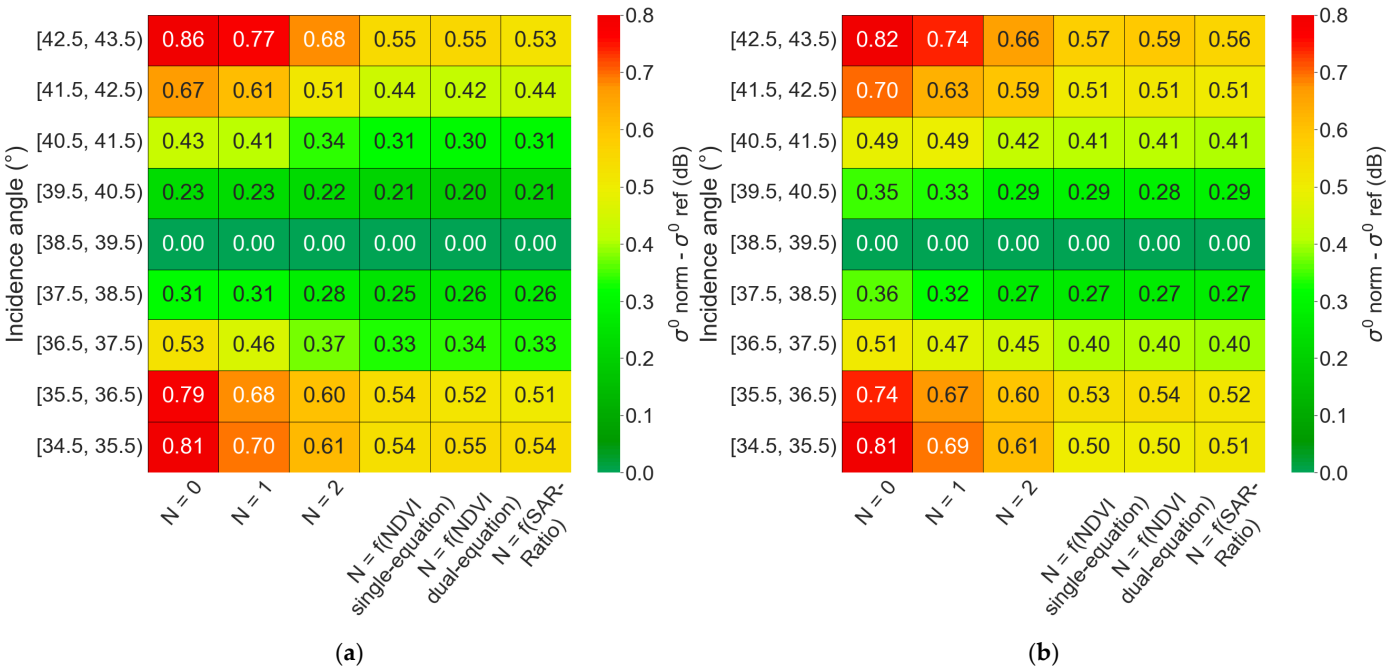

Figure 11. The mean difference between σ^0_{norm} and σ^0_{ref} by incidence angle range for orbit D8. (**a**) VV polarization; (**b**) VH polarization. N = 0 corresponds to the backscattering coefficient before normalization.

Secondly, the change in the backscattering coefficient was analyzed after normalization at certain key dates. Figure 12 quantifies the effect of normalization on the orbit D8 for the VV polarization (A30 in Appendix A) by showing the amount of change ($\Delta\sigma^0_{\mathrm{nr}}$(dB)) in the backscattering coefficient after normalization, with $\Delta\sigma^0_{\mathrm{rn}} = \left|\sigma^0(\theta) - \sigma^0_{ref}\right| - \left|\sigma^0_{norm} - \sigma^0_{ref}\right|$. $\Delta\sigma^0_{\mathrm{rn}}$ represents how much the backscattering coefficient became closer to the reference value σ^0_{ref} after normalization. For example, if σ^0 for θ = 35° before normalization was −8 dB and σ^0_{ref} for θ_{norm} = 39° was −10 dB, while σ^0 after normalization (σ^0_{norm}) was −9.5 dB, then $\Delta\sigma^0_{\mathrm{rn}}$ (dB) would be +1.5 dB, meaning that normalization reduced angular dependence by 1.5 dB (from 2 dB to 0.5 dB).

Figure 12 shows the median change for all fields in each incidence angle range in the study area for five dates. When using N = 1, Figure 12a shows that normalization leads to a maximum change of 0.25 dB when the difference in incidence angle (incidence delta) is around 4° (between the center = 39° and the western edge = 43°), meaning that normalization leads to a correction of up to 0.25 dB at most. Comparing Figures 12a and 12b shows that simple cosine-squared (N = 2) normalization performed better than first-order normalization, with a maximum improvement of 0.49 dB compared to the original backscattering data. However, all dynamic N normalization methods perform better than fixed N. Figure 12c shows that when using N = f(NDVI single-equation), the resulting maximum change is 0.83 dB, while for N = f(NDVI dual-equation), the maximum change obtained is 0.80 dB, as shown in Figure 12d. Finally, Figure 12e shows that N = f(SAR Ratio) had a maximum change of 0.79 dB for an incidence delta of around 4°. Thus, the

NDVI-based and SAR ratio-based dynamic normalization approaches deliver a similar normalization performance.

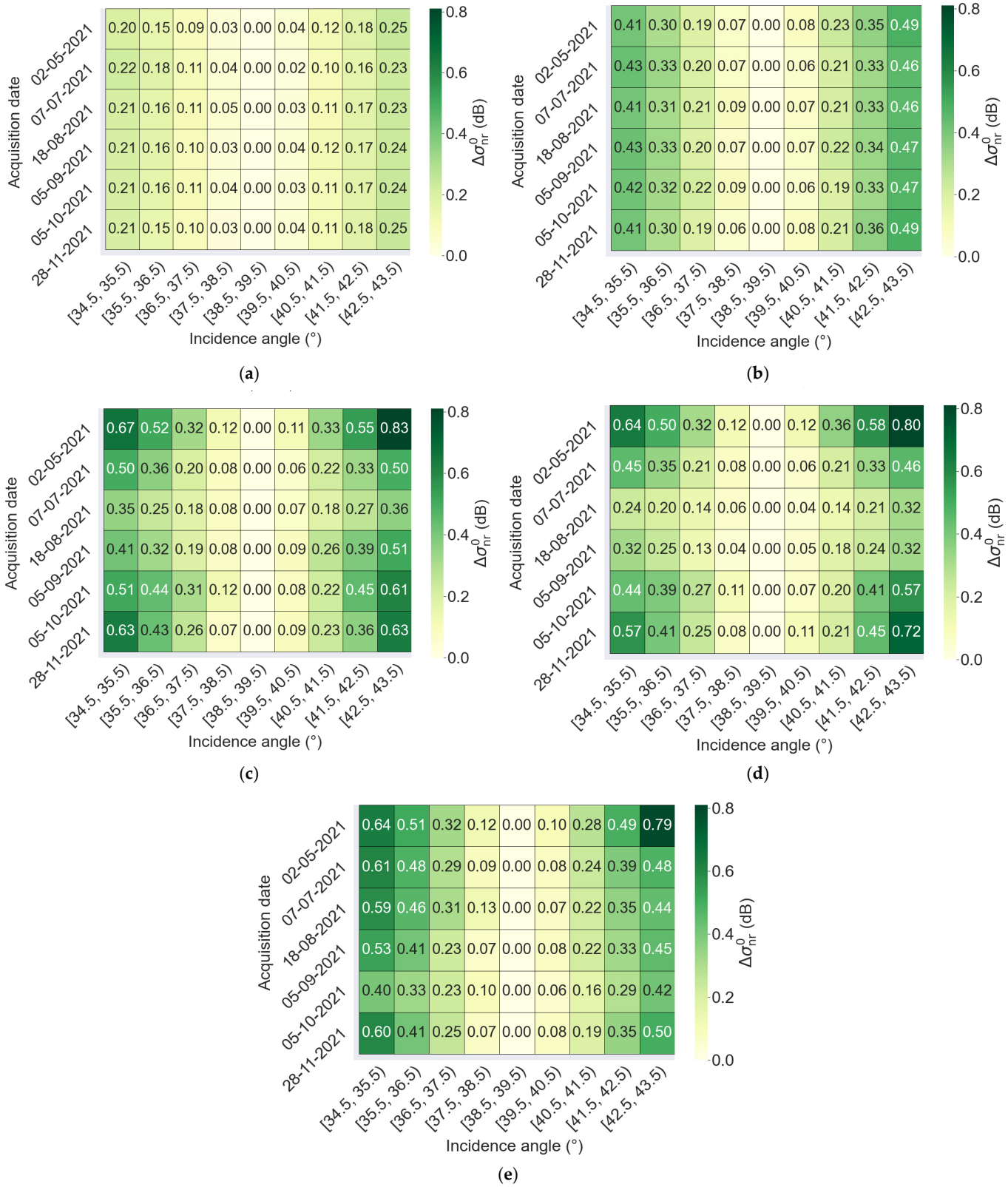

Figure 12. The change in the backscattering for orbit D8 in the VV polarization after normalization using the different approaches. (**a**) fixed N = 1; (**b**) fixed N = 2; (**c**) N = f(NDVI single-equation); (**d**) N = f(NDVI dual-equation); (**e**) N = (SAR Ratio). Results for orbit A30 in Appendix A.

The values of $\Delta\sigma^0_{rn}$ (dB) could be underestimated due to (1) N fitting errors, (2) irrigation activity, and (3) the fact that the ERA5-Land data used to eliminate S1 data acquired on surfaces that have experienced rainfall may be imprecise because of the intrinsic uncertainty of the ERA5-Land data, as well as their coarser spatial resolution (~9 km × 9 km). For example, if at a given date, there was local rainfall only on fields located around θ = 43°, then σ^0 from these fields before normalization would be higher than σ^0 from fields located close to the reference angle (39° for D8). By definition, normalizing the data between 40° and 43° will lead to an increase in σ^0 after normalization (for θ_{norm} = 39°), which is not correct in theory because σ^0 must decrease when the incidence angle increases. If this is the case, normalization will lead to a further increase in σ^0, away from σ^0_{ref}. This does not mean that normalization has led to errors, but that σ^0_{norm} cannot be compared with σ^0_{ref}, as the characteristics of the environment are not identical, as in our initial assumption. Furthermore, data corresponding to periods without vegetation, mainly the earliest dates (period before plant emergence) and the latest dates (post-harvest), generally have very heterogeneous soil characteristics, as tillage is not at the same date for all fields and neither are harvests, and as soil roughness has a strong influence on the N value. Therefore, normalization may have errors during these periods, as sometimes an N that is not adapted to the roughness of certain fields is used (N is higher for high roughness than for low roughness).

Figure 13 shows the change after normalization for the orbit D8 in VH polarization. N = 1 results in a maximum change of 0.25 dB (Figure 13) when the difference in incidence angle (incidence delta) is around 4° (between the center = 39° and the edge = 43°). Figure 13b shows that the maximum change using N = 2 is 0.50 dB. The maximum change was higher when using dynamic N methods, with maximum changes at 0.62, 0.57, and 0.59 for N = f(NDVI single-equation) (Figure 13c), N = f(NDVI dual-equation) (Figure 13d), and N = f(SAR Ratio) (Figure 13e), respectively. As for the case with the VV polarization (Figure 12), $\Delta\sigma^0_{rn}$ (dB) could be underestimated in certain sections of the S1 swath that have different properties to the rest of the extent at the same date, mainly due to precipitation, irrigation, and soil roughness.

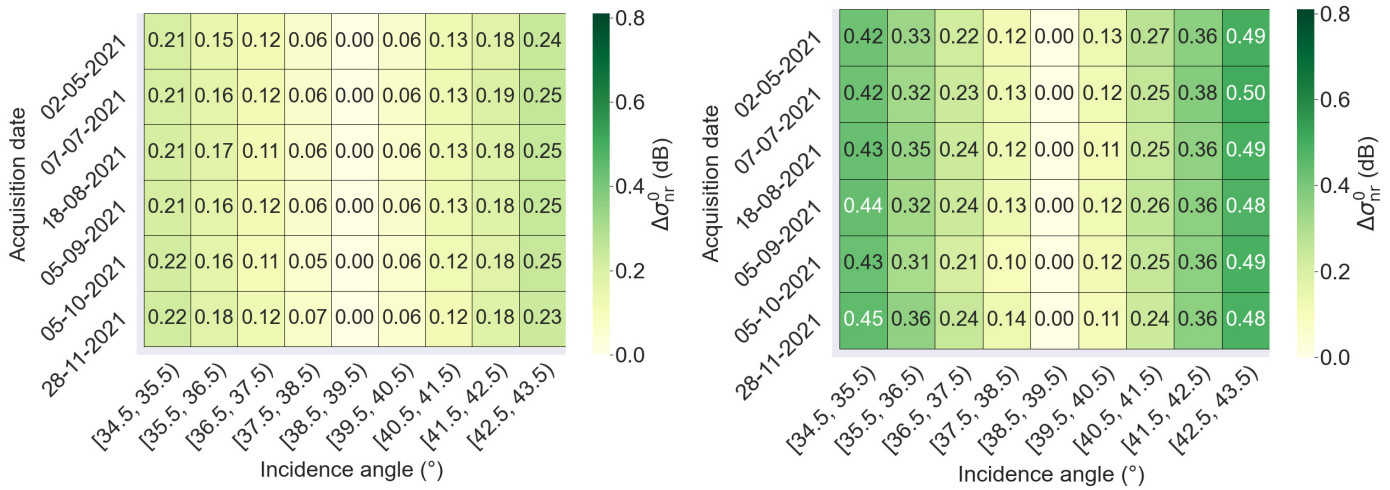

Figure 13. *Cont.*

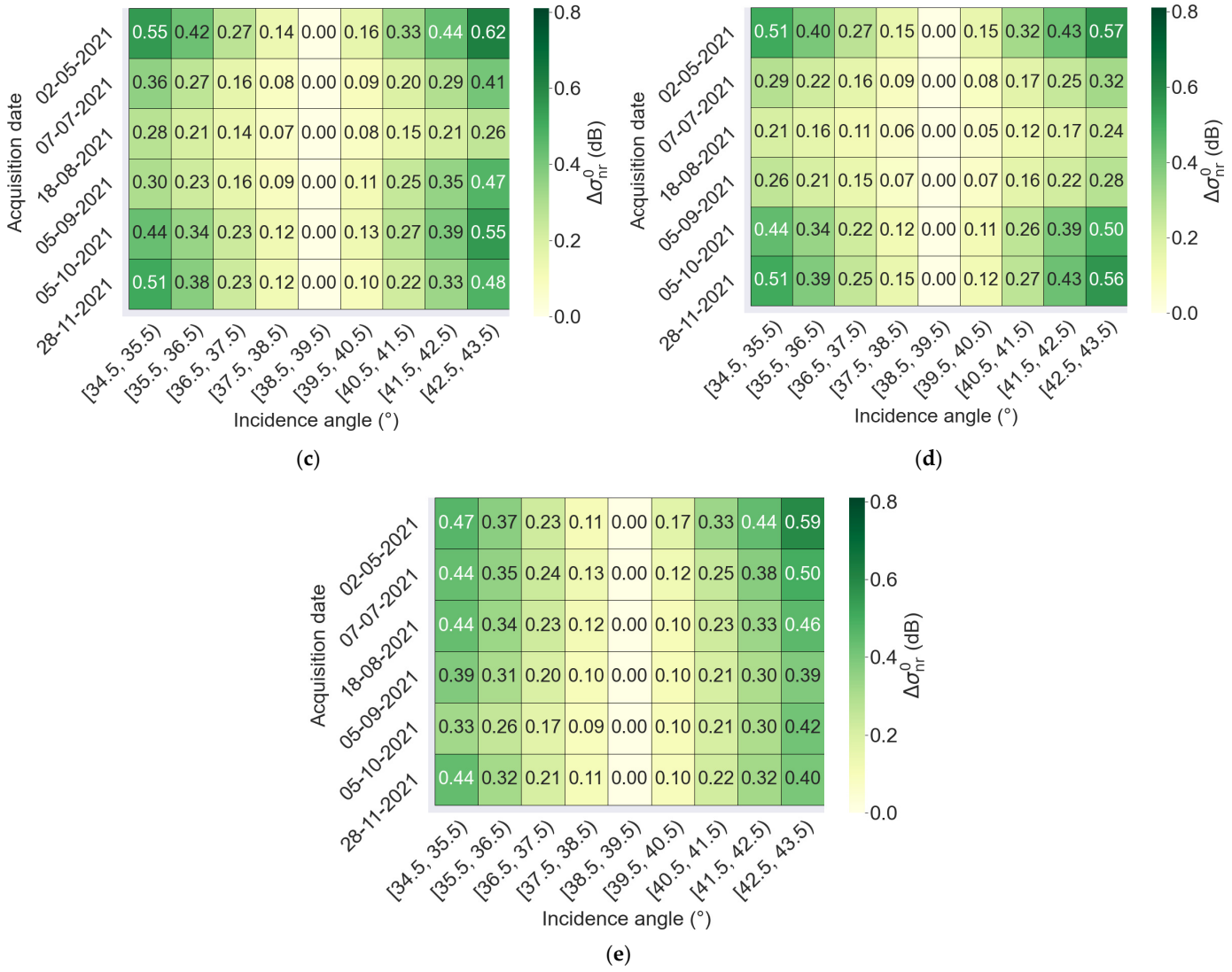

Figure 13. The change in backscattering for orbit D8 in the VH polarization after normalization using the different approaches. (**a**) fixed N = 1; (**b**) fixed N = 2; (**c**) N = f(NDVI single-equation); (**d**) N = f(NDVI dual-equation); (**e**) N = (SAR Ratio). Results for orbit A30 in Appendix A.

As shown by the results, as we move from the center of the image towards its edges, the variation in the incidence angle is greater and $\Delta\sigma^0_{rn}$ is greater, because normalization depends on the difference between θ_i and θ_{norm} (Equation (2)). That being said, it is important to note that our area only covered around a third of the width of an S1 tile. In fact, the maximum difference in incidence reaches up to around 10° (from the center to the edges) for the entirety of the S1 swath, whereas our biggest difference in incidence is 4°. Assuming that the relationship between the correction of σ^0 and the incidence angle is linear across the entire width of the S1 tile, we can expect a maximum change of around 2.0 dB for the VV polarization and 1.6 dB for the VH polarization when working over the entirety of the S1 swath (incidence delta is around 10°).

Furthermore, the normalization of σ^0 is most relevant during the vegetation growth cycle because the calculation of N only depends on the NDVI or SAR Ratio, which we can calculate, whereas this normalization before plant emergence or after harvesting could contain more uncertainty because the calculation of N requires knowledge of roughness that we cannot readily obtain.

5. Conclusions

The radar backscattering coefficient (σ^0) over a defined agricultural field for a given SAR (Synthetic Aperture Radar) sensor depends on the incidence angle, soil characteristics (mainly surface roughness), and the stage of vegetation development. The current revisit time of Sentinel-1 (S1) is typically 12 days (with one functioning satellite out of two), sometimes rendering the use of all available data over a given area (all orbits) necessary in order to improve the density of the S1 time series. Furthermore, the interpretation of S1 data acquired over a wide swath (250 km) requires high vigilance because two fields with the same crop and the same soil and vegetation characteristics would have very different σ^0 values (a difference that is generally higher than 2 dB for a 20° difference in the S1 incidence angle).

This study demonstrates that the angular dependence of the S1 σ^0 is similar for the three analyzed summer crops (sunflower, soybean, and corn), with low angular dependence during the well-developed vegetation stage. On the other hand, there are significant fluctuations in the angular dependence during the period prior to plant emergence due to the variations in soil roughness. Overall, angular dependence was slightly higher for VV than for VH polarization.

A dynamic normalization approach was applied, based on the vegetation descriptors NDVI and SAR ratio (VV/VH), leading to a decrease in the angular dependence of σ^0. This dynamic normalization was more effective compared to temporally fixed normalization, with NDVI single-equation-, NDVI dual-equation- and SAR Ratio-based dynamic normalizations yielding a similar performance. The similar performances of the SAR-based and NDVI-based dynamic normalization highlight the ability to obtain effective dynamic N normalization using only SAR data.

Furthermore, the results showed that when dynamic normalization is applied to the entire swath of an S1 acquisition, the expected correction in the backscattering coefficient is around 2.0 dB for the VV polarization and 1.6 dB for the VH polarization.

This paper shows that our normalization is most appropriate for the period corresponding to vegetation development but may be insufficient for the period corresponding to soil preparation. In fact, during this period, soil roughness information is necessary because the most successful normalization approach would require not only vegetation descriptors but also soil roughness data, whereas the latter is not readily obtainable at the operational level.

Author Contributions: Conceptualization, S.N. and N.B.; data curation, S.N.; formal analysis, S.N. and N.B.; methodology, S.N. and N.B.; software, S.N.; supervision, N.B.; validation, S.N. and N.B.; writing—original draft, S.N. and N.B.; writing—review and editing, N.B., H.B. and M.Z. All authors have read and agreed to the published version of the manuscript.

Funding: This research received funding from the French Space Study Center (CNES, TOSCA 2022 project), the French Agency for Ecological Transition (ADEME, RSEAU project) and the National Research Institute for Agriculture, Food and the Environment (INRAE).

Data Availability Statement: The data used in this work are open source and freely available.

Acknowledgments: The authors wish to thank the French Space Study Center (CNES, TOSCA 2022), the French Agency for Ecological Transition (ADEME, RSEAU project) and the National Research Institute for Agriculture, Food and the Environment (INRAE) for supporting this work. The authors would also like to thank the European Space Agency (ESA) for providing the Sentinel-1 images and the French Land Data Center (Theia) for providing the Sentinel-2 images.

Conflicts of Interest: The authors declare no conflicts of interest.

Appendix A

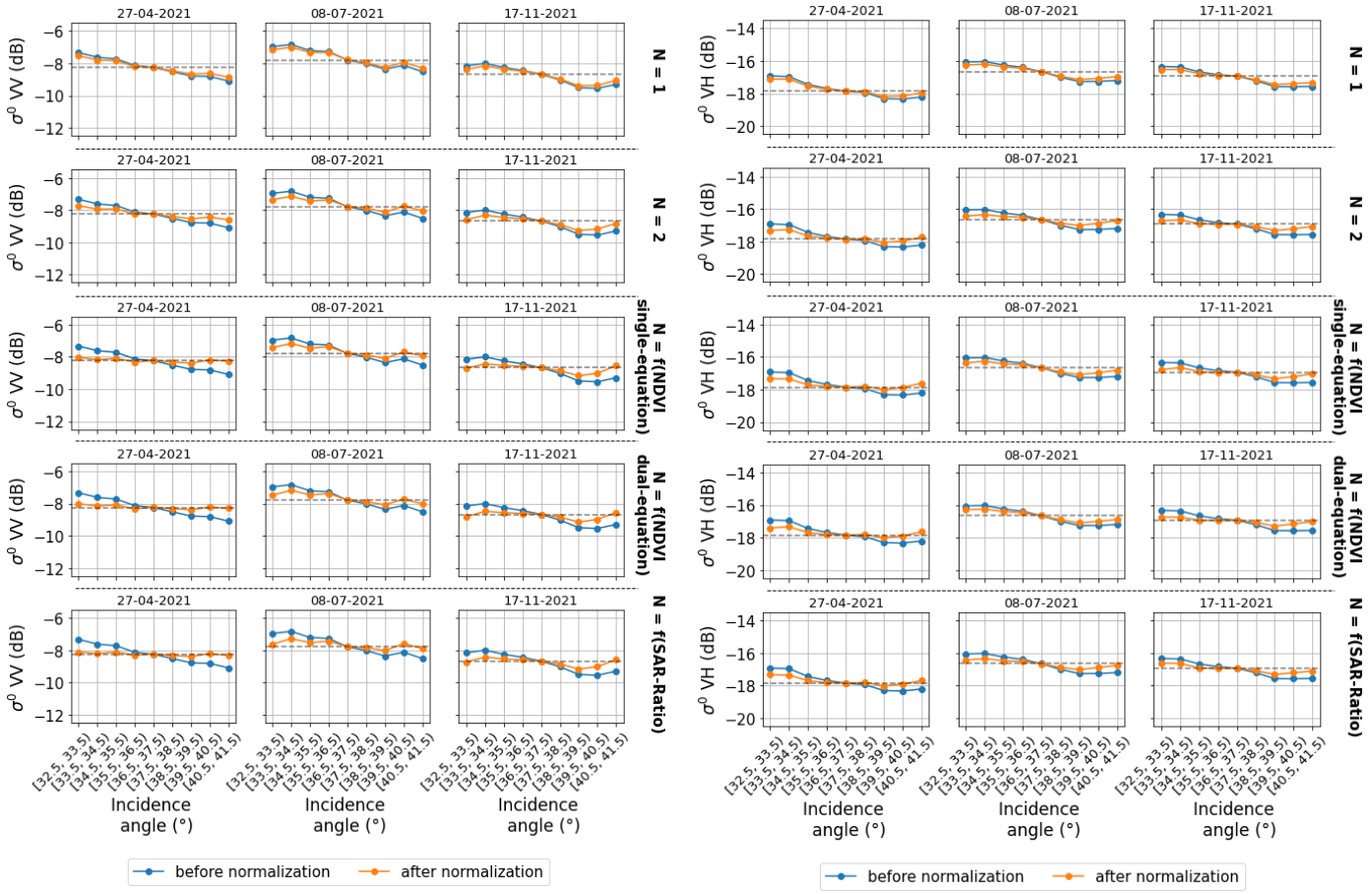

(**a**) (**b**)

Figure A1. Comparison of the backscattering coefficient before and after normalization to θ_{norm} = 37° for orbit A30. One row is used to represent each approach: fixed N = 1, fixed N = 2, N = f(NDVI single-equation), N = f(NDVI dual-equation), N = (SAR Ratio). The dotted line corresponds to σ^0 at θ=39°, called σ^0_{ref}. (**a**): VV, (**b**): VH.

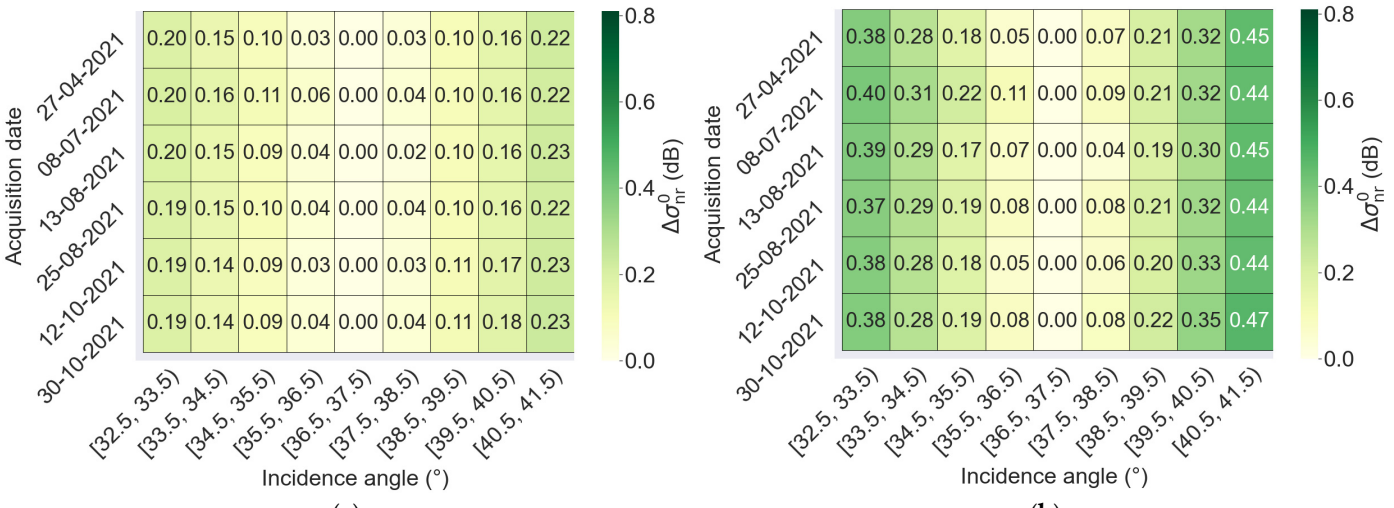

(**a**) (**b**)

Figure A2. *Cont.*

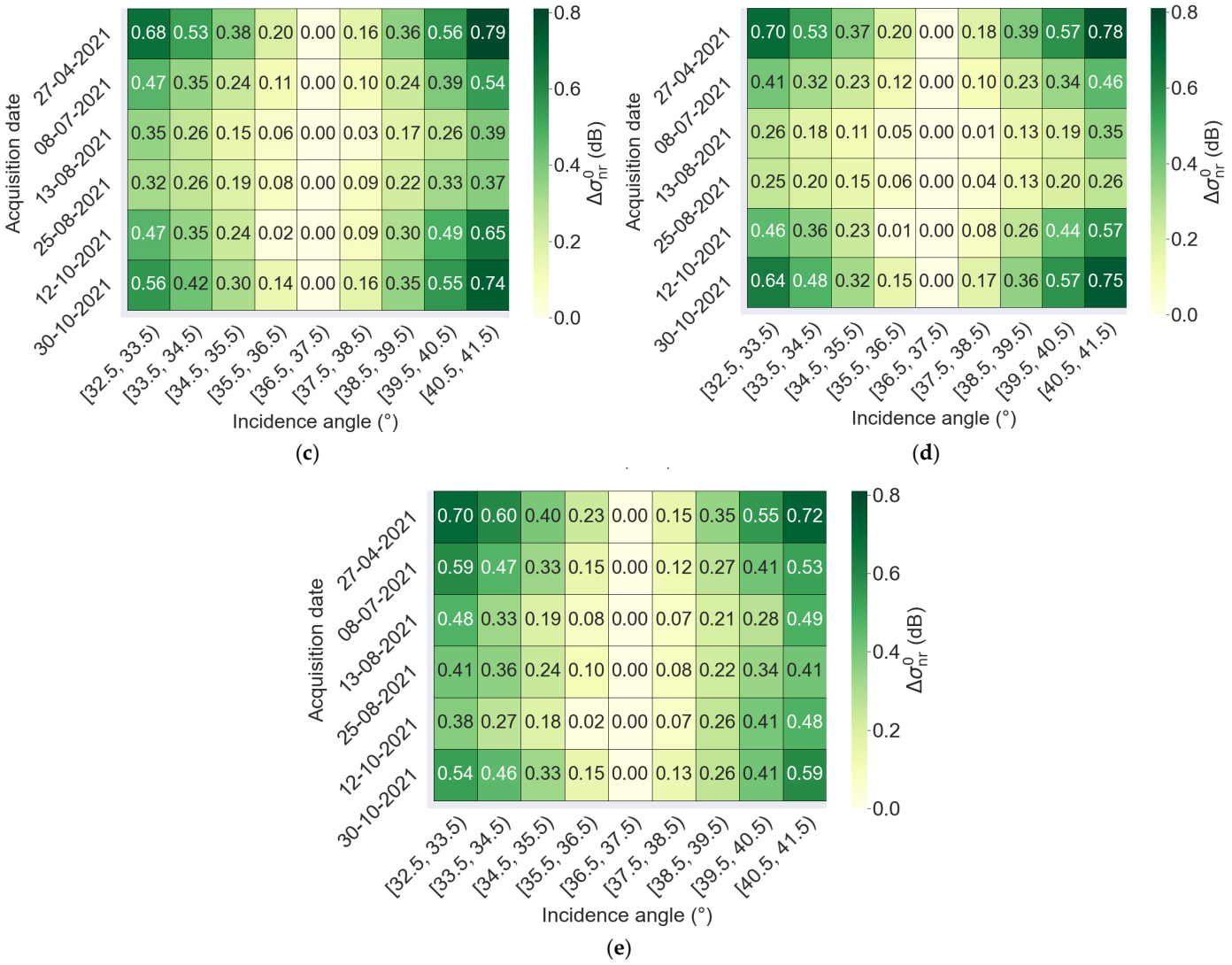

Figure A2. The change in the backscattering for orbit A30 in the VV polarization after normalization using the different approaches: (**a**) fixed N = 1; (**b**) fixed N = 2; (**c**) N = f(NDVI single-equation); (**d**) N = f(NDVI dual-equation); (**e**) N = (SAR Ratio).

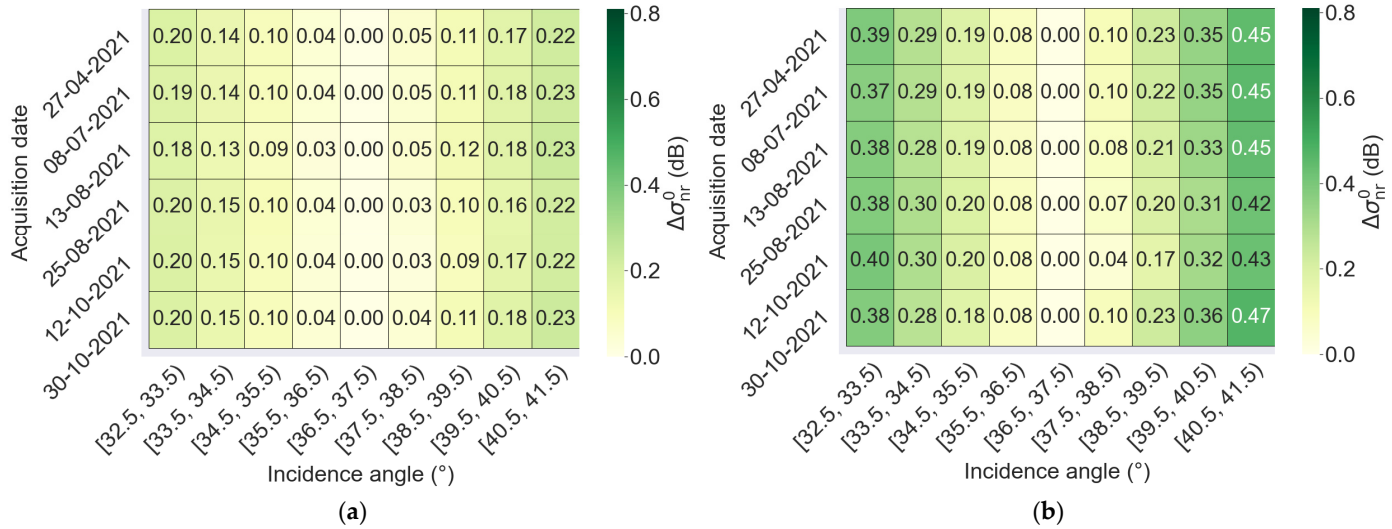

Figure A3. *Cont.*

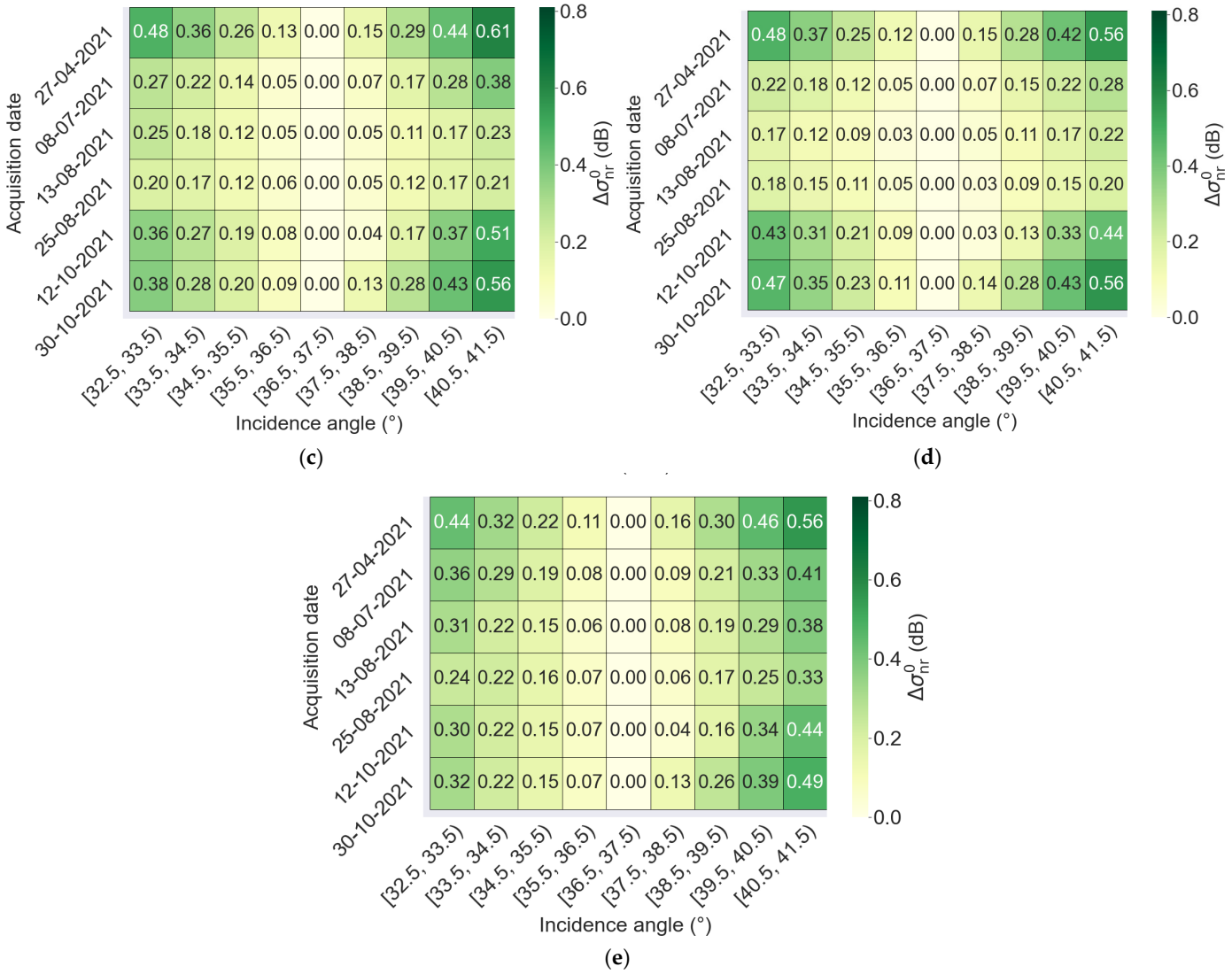

Figure A3. The change in the backscattering for orbit A30 in the VH polarization after normalization using the different approaches: (**a**) fixed N = 1; (**b**) fixed N = 2; (**c**) N = f(NDVI single-equation); (**d**) N = f(NDVI dual-equation); (**e**) N = (SAR Ratio).

References

1. Torres, R.; Snoeij, P.; Geudtner, D.; Bibby, D.; Davidson, M.; Attema, E.; Potin, P.; Rommen, B.; Floury, N.; Brown, M.; et al. GMES Sentinel-1 mission. *Remote Sens. Environ.* **2012**, *120*, 9–24. [CrossRef]
2. Betbeder, J.; Rapinel, S.; Corgne, S.; Pottier, E.; Hubert-Moy, L. TerraSAR-X dual-pol time-series for mapping of wetland vegetation. *ISPRS J. Photogramm. Remote Sens.* **2015**, *107*, 90–98. [CrossRef]
3. Maleki, S.; Baghdadi, N.; Dantas, C.F.; Najem, S.; Bazzi, H.; Reluy, N.P.; Ienco, D.; Zribi, M. Artificial Intelligence Algorithms for Rapeseed Fields Mapping Using Sentinel-1 Time Series: Temporal Transfer Scenario and Ground Sampling Constraints. *IEEE J. Sel. Top. Appl. Earth Obs. Remote Sens.* **2023**, *16*, 8884–8899. [CrossRef]
4. Najem, S.; Baghdadi, N.; Bazzi, H.; Lalande, N.; Bouchet, L. Detection and Mapping of Cover Crops using Sentinel-1 SAR Remote Sensing data. *IEEE J. Sel. Top. Appl. Earth Obs. Remote Sens.* **2023**, *17*, 1446–1461. [CrossRef]
5. Bazzi, H.; Baghdadi, N.; Najem, S.; Jaafar, H.; Le Page, M.; Zribi, M.; Faraslis, I.; Spiliotopoulos, M. Detecting Irrigation Events over Semi-Arid and Temperate Climatic Areas Using Sentinel-1 Data: Case of Several Summer Crops. *Agronomy* **2022**, *12*, 2725. [CrossRef]
6. Bazzi, H.; Baghdadi, N.; El Hajj, M.; Zribi, M.; Belhouchette, H. A Comparison of Two Soil Moisture Products S2MP and Copernicus-SSM Over Southern France. *IEEE J. Sel. Top. Appl. Earth Obs. Remote Sens.* **2019**, *12*, 3366–3375. [CrossRef]
7. Dimov, D.; Löw, F.; Ibrakhimov, M.; Stulina, G.; Conrad, C. SAR and optical time series for crop classification. In Proceedings of the 2017 IEEE International Geoscience and Remote Sensing Symposium (IGARSS), Fort Worth, TX, USA, 23–28 July 2017; pp. 811–814.

8. Shi, J.; Dozier, J. Estimation of snow water equivalence using SIR-C/X-SAR. I. Inferring snow density and subsurface properties. *IEEE Trans. Geosci. Remote Sens.* **2000**, *38*, 2465–2474. [CrossRef]
9. Wang, Y.; Day, J.L.; Davis, F.W.; Melack, J.M. Modeling L-band radar backscatter of Alaskan boreal forest. *IEEE Trans. Geosci. Remote Sens.* **1993**, *31*, 1146–1154. [CrossRef]
10. Aldenhoff, W.; Eriksson, L.E.B.; Ye, Y.; Heuzé, C. First-Year and Multiyear Sea Ice Incidence Angle Normalization of Dual-Polarized Sentinel-1 SAR Images in the Beaufort Sea. *IEEE J. Sel. Top. Appl. Earth Obs. Remote Sens.* **2020**, *13*, 1540–1550. [CrossRef]
11. Zribi, M.; Baghdadi, N.; Holah, N.; Fafin, O. New methodology for soil surface moisture estimation and its application to ENVISAT-ASAR multi-incidence data inversion. *Remote Sens. Environ.* **2005**, *96*, 485–496. [CrossRef]
12. Gill, J.P.S.; Yackel, J.J.; Geldsetzer, T.; Fuller, M.C. Sensitivity of C-band synthetic aperture radar polarimetric parameters to snow thickness over landfast smooth first-year sea ice. *Remote Sens. Environ.* **2015**, *166*, 34–49. [CrossRef]
13. Mäkynen, M.; Karvonen, J. Incidence Angle Dependence of First-Year Sea Ice Backscattering Coefficient in Sentinel-1 SAR Imagery Over the Kara Sea. *IEEE Trans. Geosci. Remote Sens.* **2017**, *55*, 6170–6181. [CrossRef]
14. Komarov, A.S.; Buehner, M. Detection of First-Year and Multi-Year Sea Ice from Dual-Polarization SAR Images Under Cold Conditions. *IEEE Trans. Geosci. Remote Sens.* **2019**, *57*, 9109–9123. [CrossRef]
15. Makynen, M.P.; Manninen, A.T.; Simila, M.H.; Karvonen, J.A.; Hallikainen, M.T. Incidence angle dependence of the statistical properties of C-band HH-polarization backscattering signatures of the Baltic Sea ice. *IEEE Trans. Geosci. Remote Sens.* **2002**, *40*, 2593–2605. [CrossRef]
16. Paluba, D.; Laštovička, J.; Mouratidis, A.; Štych, P. Land Cover-Specific Local Incidence Angle Correction: A Method for Time-Series Analysis of Forest Ecosystems. *Remote Sens.* **2021**, *13*, 1743. [CrossRef]
17. Mladenova, I.E.; Jackson, T.J.; Bindlish, R.; Hensley, S. Incidence Angle Normalization of Radar Backscatter Data. *IEEE Trans. Geosci. Remote Sens.* **2013**, *51*, 1791–1804. [CrossRef]
18. Feng, Z.; Zheng, X.; Li, L.; Li, B.; Chen, S.; Guo, T.; Wang, X.; Jiang, T.; Li, X.; Li, X. Dynamic Cosine Method for Normalizing Incidence Angle Effect on C-band Radar Backscattering Coefficient for Maize Canopies Based on NDVI. *Remote Sens.* **2021**, *13*, 2856. [CrossRef]
19. Hoekman, D.H.; Reiche, J. Multi-model radiometric slope correction of SAR images of complex terrain using a two-stage semi-empirical approach. *Remote Sens. Environ.* **2015**, *156*, 1–10. [CrossRef]
20. Small, D. Flattening Gamma: Radiometric Terrain Correction for SAR Imagery. *IEEE Trans. Geosci. Remote Sens.* **2011**, *49*, 3081–3093. [CrossRef]
21. Zhao, L.; Chen, E.; Li, Z.; Zhang, W.; Gu, X. Three-Step Semi-Empirical Radiometric Terrain Correction Approach for PolSAR Data Applied to Forested Areas. *Remote Sens.* **2017**, *9*, 269. [CrossRef]
22. Lang, W.; Zhang, P.; Wu, J.; Shen, Y.; Yang, X. Incidence Angle Correction of SAR Sea Ice Data Based on Locally Linear Mapping. *IEEE Trans. Geosci. Remote Sens.* **2016**, *54*, 3188–3199. [CrossRef]
23. Widhalm, B.; Bartsch, A.; Goler, R. Simplified Normalization of C-Band Synthetic Aperture Radar Data for Terrestrial Applications in High Latitude Environments. *Remote Sens.* **2018**, *10*, 551. [CrossRef]
24. Ulaby, F.T.; Moore, R.K.; Fung, A.K. *Microwave Remote Sensing: Active and Passive. Volume 2-Radar Remote Sensing and Surface Scattering and Emission Theory*; Artech House: Norwood, MA, USA, 1982.
25. Topouzelis, K.; Singha, S.; Kitsiou, D. Incidence angle normalization of Wide Swath SAR data for oceanographic applications. *Open Geosci.* **2016**, *8*, 450–464. [CrossRef]
26. Ardila, J.P.; Tolpekin, V.; Bijker, W. Angular Backscatter Variation in L-Band ALOS ScanSAR Images of Tropical Forest Areas. *IEEE Geosci. Remote Sens. Lett.* **2010**, *7*, 821–825. [CrossRef]
27. Clapp, R.E. *A Theoretical and Experimental Study of Radar Ground Return*; Radiation Laboratory, Massachusetts Institute of Technology: Cambridge, MA, USA, 1946.
28. Guo, H. Digital Earth: Big Earth Data. *Int. J. Digit. Earth* **2014**, *7*, 1–2. [CrossRef]
29. Zribi, M.; Chahbi, A.; Shabou, M.; Lili-Chabaane, Z.; Duchemin, B.; Baghdadi, N.; Amri, R.; Chehbouni, A. Soil surface moisture estimation over a semi-arid region using ENVISAT ASAR radar data for soil evaporation evaluation. *Hydrol. Earth Syst. Sci.* **2011**, *15*, 345–358. [CrossRef]
30. Baghdadi, N.; Bernier, M.; Gauthier, R.; Neeson, I. Evaluation of C-band SAR data for wetlands mapping. *Int. J. Remote Sens.* **2001**, *22*, 71–88. [CrossRef]
31. Van Doninck, J.; Wagner, W.; Melzer, T.; De Baets, B.; Verhoest, N.E.C. Seasonality in the Angular Dependence of ASAR Wide Swath Backscatter. *IEEE Geosci. Remote Sens. Lett.* **2014**, *11*, 1423–1427. [CrossRef]
32. Fieuzal, R.; Baup, F.; Marais-Sicre, C. Monitoring Wheat and Rapeseed by Using Synchronous Optical and Radar Satellite Data—From Temporal Signatures to Crop Parameters Estimation. *Adv. Remote Sens.* **2013**, *2*, 162–180. [CrossRef]
33. Cristea, A.; van Houtte, J.; Doulgeris, A.P. Integrating Incidence Angle Dependencies Into the Clustering-Based Segmentation of SAR Images. *IEEE J. Sel. Top. Appl. Earth Obs. Remote Sens.* **2020**, *13*, 2925–2939. [CrossRef]
34. Huete, A.R.; Liu, H.Q. An error and sensitivity analysis of the atmospheric- and soil-correcting variants of the NDVI for the MODIS-EOS. *IEEE Trans. Geosci. Remote Sens.* **1994**, *32*, 897–905. [CrossRef]
35. Leprieur, C.; Kerr, Y.H.; Mastorchio, S.; Meunier, J.C. Monitoring vegetation cover across semi-arid regions: Comparison of remote observations from various scales. *Int. J. Remote Sens.* **2000**, *21*, 281–300. [CrossRef]

36. Shu, M.; Zhou, L.; Gu, X.; Ma, Y.; Sun, Q.; Yang, G.; Zhou, C. Monitoring of maize lodging using multi-temporal Sentinel-1 SAR data. *Adv. Space Res.* **2020**, *65*, 470–480. [CrossRef]
37. Mandal, D.; Kumar, V.; Ratha, D.; Dey, S.; Bhattacharya, A.; Lopez-Sanchez, J.M.; McNairn, H.; Rao, Y.S. Dual polarimetric radar vegetation index for crop growth monitoring using sentinel-1 SAR data. *Remote Sens. Environ.* **2020**, *247*, 111954. [CrossRef]
38. Ayari, E.; Kassouk, Z.; Lili-Chabaane, Z.; Ouaadi, N.; Baghdadi, N.; Zribi, M. NDVI estimation using Sentinel-1 data over wheat fields in a semiarid Mediterranean region. *GIScience Remote Sens.* **2024**, *61*, 2357878. [CrossRef]
39. Rolle, M.; Tamea, S.; Claps, P.; Ayari, E.; Baghdadi, N.; Zribi, M. Analysis of Maize Sowing Periods and Cycle Phases Using Sentinel 1&2 Data Synergy. *Remote Sens.* **2022**, *14*, 3712. [CrossRef]
40. Shi, J.; Dozier, J.; Rott, H. Snow mapping in alpine regions with synthetic aperture radar. *IEEE Trans. Geosci. Remote Sens.* **1994**, *32*, 152–158. [CrossRef]
41. Qadir, G.; Fayyaz-ul-Hassan; Malik, M.A. Growing degree days and yield relationship in sunflower (*Helianthus annuus* L.). *Int. J. Agric. Biol. Pak.* **2007**, *9*, 564–568.
42. Hajj, M.E.; Baghdadi, N.; Belaud, G.; Zribi, M.; Cheviron, B.; Courault, D.; Hagolle, O.; Charron, F. Irrigated Grassland Monitoring Using a Time Series of TerraSAR-X and COSMO-SkyMed X-Band SAR Data. *Remote Sens.* **2014**, *6*, 10002–10032. [CrossRef]
43. He, B.; Xing, M.; Bai, X. A Synergistic Methodology for Soil Moisture Estimation in an Alpine Prairie Using Radar and Optical Satellite Data. *Remote Sens.* **2014**, *6*, 10966–10985. [CrossRef]